The Pennsylvania State University

The Graduate School

College of Engineering

INVESTIGATION OF SOLID OXIDIZER AND GASEOUS FUEL COMBUSTION

PERFORMANCE USING AN ELEVATED PRESSURE COUNTERFLOW

EXPERIMENT AND REVERSE HYBRID ROCKET ENGINE

A Thesis in

Aerospace Engineering

by

Reed H. Johansson

Submitted in Partial Fulfillment
of the Requirements
for the Degree of

Master of Science

August 2012

The thesis of Reed H. Johansson was reviewed and approved* by the following:

Richard A. Yetter
Professor of Mechanical Engineering
Thesis Co-Adviser

Grant A. Risha
Associate Professor of Mechanical Engineering
Thesis Co-Adviser

Cengiz Camci
Professor of Aerospace Engineering

George A. Lesieutre
Professor of Aerospace Engineering
Head of the Department of Aerospace Engineering

*Signatures are on file in the Graduate School.

Abstract

Pressurized counterflow and static-fired motor studies were conducted to explore the possibility of a reverse hybrid system, having a solid oxidizer and gaseous fuel. Theoretical performance analysis indicates such a system may yield specific impulse and density specific impulse similar to composite solid propellants, yet with the added capability to throttle, shut down, and restart firings. Pressurized counterflow studies conducted using pressed ammonium perchlorate pellets and gaseous ethylene show three pressure dependent combustion regimes. At pressures below 1 MPa, ammonium perchlorate decomposition is controlled by heat transfer from the resulting fuel/oxidizer diffusion flame, exhibiting a weak dependence on flame strain rate and burning rates between 0.01 to 0.05 cm/s. As pressure increases, the monopropellant flame moves closer to the oxidizer surface until the pressure reaches the self-decomposition limit near 3 MPa, indicating that the monopropellant flame dominates the diffusion flame. Further increasing the pressure yields burning rates between 0.4 to 0.7 cm/s, which are consistent with the literature, and exhibit little strain rate dependence for the range of flow conditions tested. Similar studies conducted with methane suggest independence of fuel type. The pressurized counterflow apparatus was also utilized to examine the regression rate of hydroxyl-terminated polybutadiene with gaseous oxygen at varied pressures. The diffusion-controlled burning rates exhibited no pressure dependence, as expected, and agreed well with published regression rate data. Lab-scale static reverse hybrid rocket motor firings focused on the mid- to high-pressure combustion regime, examining ignition and system operating parameters. Results indicate that combustion is highly dependent on the initial pressure of the motor, producing a fast burn with initial pressures of 4.45 and 2.20 MPa, while behaving like a gas generator at a lower initial pressure of 1.14 MPa. Analysis also suggests that there is a minimum fuel flow requirement, below which the motor would not operate in the high pressure and burning rate regime.

Table of Contents

List of Figures

List of Tables

Acknowledgements

Chapter 1

Introduction

1.1   Hybrid history

Hybrid rocket propulsive systems have been considered for many years as the physical separation of the fuel and oxidizer promotes an inherent safety [1]. Classically, these systems employ an inert solid fuel grain stored within the combustion chamber and an oxidizer that is pumped through a porting within the fuel grain at the time of ignition [2], permitting throttling by variation of oxidizer flow rate. Once ignited, pyrolyzed fuel mixes and combusts with the injected oxidizer, forming a diffusion flame, as depicted in Figure 1.1.   The high temperature/pressure combustion products are then exhausted through a nozzle generating thrust. By comparison, a "reverse hybrid" system utilizes a liquid or gaseous fuel and an oxidizer [3], or perhaps a monopropellant, as the solid phase component. In the latter case, combustion may be governed by two different flames, shown in Figure 1.2, as the oxidizer burns with a pressure-dependent monopropellant flame, the products of which combust with injected fuel forming a pressure-independent diffusion flame [4].
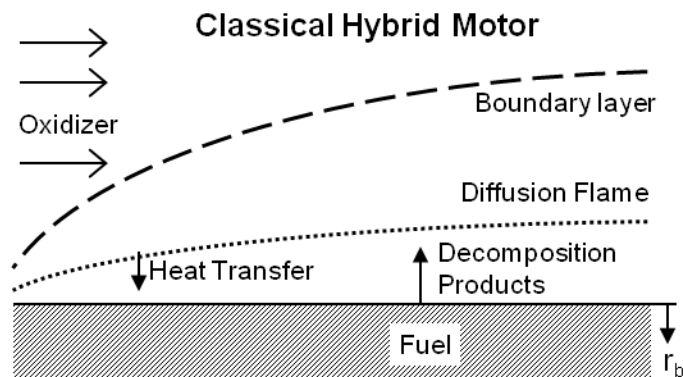
Figure 1.1. Classical hybrid combustion schematic.
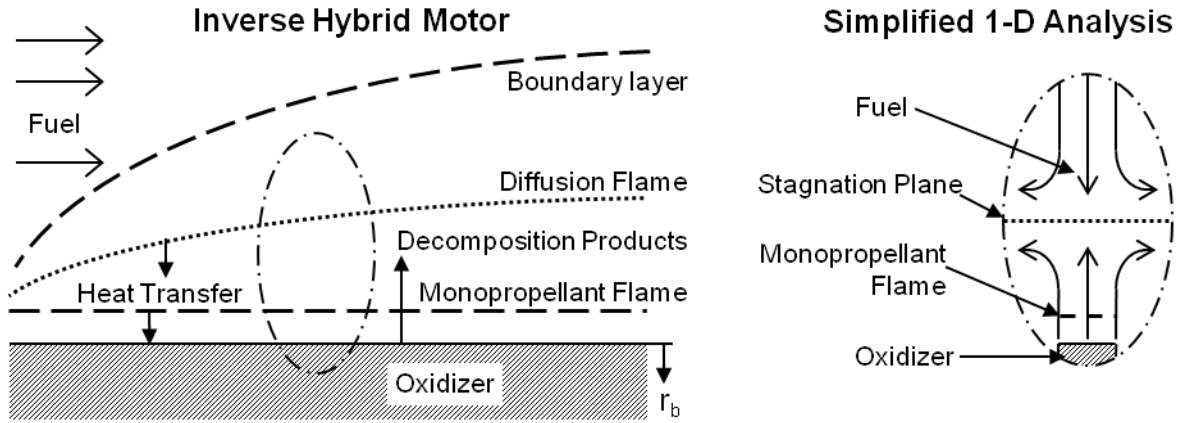
Figure 1.2. Reverse hybrid combustion schematic and 1-dimensional analogue for counterflow system analysis.

Classical hybrid systems often suffer from low fuel regression rates and reduced propellant mass fractions, due to the potential volume requirements of cryogenic storage and the low densities of the reactants, as evidenced by the example of a hybrid using inert hydroxyl-terminated polybutadiene (HTPB) as the solid fuel and liquid oxygen (LOX) as the oxidizer (with densities of 920 kg/m^3 [5] and 1150 kg/m^3 [6] respectively). Metallic additives may be introduced to the fuel to improve the density, burning rate, and the overall propulsive performance of the system [7-10]. The addition of metal hydrides [11] and more exotic energetic additives such as triaminoguanidium azotetrazolate (TAGzT) [12] have been more recently considered as means to improve performance. Furthermore, the oxidizer may be replaced with one of a non-cryogenic nature or even with a monopropellant such as hydrogen peroxide, although long-term storability issues and instability due to contamination make the use of this alternative hazardous [7]. Research has also been conducted to increase hybrid fuel regression rates by utilizing high burning rate, non-polymeric fuels, such as paraffins, which form burning droplets of fuel in the combustion chamber [13, 14]. Improvements to the low regression rates of

classical hybrid fuels have also been explored through the use of mixed hybrids, where adding small amounts of ammonium perchlorate (AP) to HTPB fuel, for example, can produce significant increases in the fuel regression rate [15, 16].

Reverse hybrid systems have been explored by several researchers in the last several decades, as the propellant mass fraction may be increased by using a high-density oxidizer, such as AP (with a density of 1950 kg/m^3 [5]), and a non-cryogenic liquid fuel, as suggested by Young *et al*. [17]. Sims and Christensen examined a binderless ammonium perchlorate/lithium perchlorate/aluminum grain which was reacted with hydrazine, though they achieved little success with that system [3]. Bennet also proposed an inverse hybrid rocket system in which the injected fuel reacts hypergolically with the solid oxidizer, however little experimental data or analysis was presented [18, 19]. A reverse/mixed hybrid system utilizing an AP/aluminum/binder grain reacting with injected hydrazine was suggested by Kaufman *et al*., with some experimental results and sample formulations being presented [20]. A slightly different reverse hybrid concept was examined by Chu, utilizing a collapsible gelled hydrazine fuel tank and thrust chambers filled with granulated oxidizer, whereby pumping fuel into these chambers would initiate gas-generating reactions which could then produce thrust [21]. Exploring reverse hybrids with non-hypergolic fuel, Ortolani *et al*. presented results from a semi-reverse hybrid that utilized a solid oxidizer combusted with injected oxygen and kerosene, briefly examining the pressure dependency of the oxidizer burning rate [22]. More recently, Peretz *et al*. explored the potential performance of a reverse hybrid with a solid grain composed of AP and potassium perchlorate particles and a Viton binder, with the potential for metallic particle addition, combusted with hydrazine [23]. Testing resulted in successful hypergolic ignition, high combustion efficiency, and stop-start capability. Cryogenic solids have also

3

recently been explored for hybrid propulsion, with research efforts being devoted to solid oxygen and gaseous hydrogen, solid hydrogen and gaseous oxygen (GOX), solid methane and GOX, and solid methane-aluminum and GOX [24].

1.2   Performance Analysis

To examine combustion characteristics of a typical reverse hybrid configuration, a simple performance analysis was conducted considering AP as the solid oxidizer and several common hydrocarbon (HC) fuels including ethylene, n-butane, and RP-1 (kerosene). As a means of comparison, the classical HTPB/LOX system is provided, as well as an HTPB/AP composite solid propellant formulation (neglecting curing agents, plasticizers, burn rate modifiers, and etcetera).   Calculations   were   performed   using   the   chemical   equilibrium   with   applications program (CEA) [25], using a chamber pressure of 6.89 MPa (1000 psia), an ideal expansion, and the conditions specified in Table 1.1. Tabulated mass fractions and volume ratios, normalized to the HTPB/LOX system, provide insight into mass and volume requirements of the fuel and oxidizer, such that values less than one imply reduced mass or volume fractions while values greater than unity indicate the opposite. From a system performance perspective, reduced volume fractions from decreased structural mass or greater propellant mass for an equivalent volume may permit increased payload capacity or yield a greater final velocity [26].

Table 1.1. Theoretical performance comparative analysis of classical hybrid and composite systems and reverse hybrid configurations.

	HTPB/LOX	Ethylene/AP	RP-1/AP	n-Butane/AP	HTPB/AP
Fuel Properties					
Chemical Formula [1]	$C_{10}H_{15.4}O_{0.07}$	C_2H_4	$C_{10}H_{19.53}$	C_4H_{10}	$C_{10}H_{15.4}O_{0.07}$
Molecular Weight [kg/kmol] [1]	136.752	28.054	139.795	58.123	136.752
Enthalpy of formation [kcal/mol]	-12.40 [1]	8.11 [3]	-56.00 [1]	-36.01 [3]	-12.40 [1]
Phase	Solid	Liquid	Liquid	Liquid	Solid
Temperature [K]	298.15	169.45	298.15	272.6	298.15
Density [kg/m^3]	920 [1]	567.6 [2]	810 [1]	601.3 [2]	920 [1]
Oxidizer Properties					
Chemical Formula [1]	O_2	ClO_4NH_4	ClO_4NH_4	ClO_4NH_4	ClO_4NH_4
Molecular Weight [kg/kmol] [1]	31.999	117.49	117.49	117.49	117.49
Enthalpy of formation [kcal/mol] [3]	-3.10	-70.69	-70.69	-70.69	-70.69
Phase	Liquid	Solid	Solid	Solid	Solid
Temperature [K]	90.19	298.15	298.15	298.15	298.15
Density [kg/m^3]	1150 [2]	1950 [1]	1950 [1]	1950 [1]	1950 [1]
Performance Comparison					
Fuel Mass Fraction	0.333	0.106	0.096	0.090	0.100
Oxidizer Mass Fraction	0.667	0.894	0.904	0.910	0.900
Fuel mass fraction Normalized to HTPB Mass Fraction	1	0.319	0.287	0.270	0.299
Oxidizer Mass Fraction Normalized to LOX Mass Fraction	1	1.340	1.357	1.365	1.350
Fuel Volume Ratio ($V_{fuel,i}/V_{HTPB}$)	1	0.517	0.326	0.413	0.299
Oxidizer Volume Ratio ($V_{ox,i}/V_{LOX}$)	1	0.784	0.793	0.798	0.789
O/F Ratio Considered [moles, (mass)]	8.55 (2)	2 (8.4)	11.25 (9.46)	5 (10.1)	10.5 (9.02)
Pressure [MPa, (psia)]	6.893 (1000)	6.893 (1000)	6.893 (1000)	6.893 (1000)	6.893 (1000)
Pressure Ratio ($P_{chamber}/P_{back}$)	68.027	68.027	68.027	68.027	68.027
Ideal Expansion Ratio (A_{exit}/A_{throat}) [3]	8.8691	8.9834	9.2459	9.2536	9.3716
Combustion Temperature [K] [3]	3576.25	3077.2	3000.97	2979.32	3031.98
Average Product MW [kg/kmol]	22.3	25.6	26.4	26.0	26.8
Characteristic Velocity (C*) [m/s] [3]	1800.7	1566.9	1527.1	1532.5	1524.5
Specific Impulse (Isp) [s] [3]	294.3	256.7	251.9	252.8	252.1
Vacuum Specific Impulse (vIsp) [s] [3]	318.2	277.8	273.0	274.0	273.5
Density Specific Impulse (ρIsp) [kg-s/m^3]	312358.5	397570.0	432849.4	410091.9	442152.0

[1] Values obtained from ICT Database of Thermochemical Values [5].

[2] Values obtained online from NIST WebBook [6].

[3] Values obtained using NASA CEA chemical equilibrium with applications program [25].

Examining the HC/AP systems, the AP decomposition products, which contain approximately 29% oxygen by volume, are mixed and reacted with fuel supplied in the reverse hybrid system resulting in a reduced fuel mass fraction compared to the baseline case. This reduction in mass fraction is evident in the normalized fuel mass fractions presented in Table 1.1 and is beneficial to system performance since the lower densities of HC fuels require relatively large storage volumes. Long-term storage capabilities and reductions in structural mass are also gained from the ability to liquefy HC fuels at low pressures without the need for cryogenic storage or cooling considerations. While HC/AP systems require significantly greater mass fractions of oxidizer than the HTPB/LOX system, the high density of AP results in reduced volume ratios. Though the oxidizer in the HC/AP systems can behave as a monopropellant, its relatively inert (non-self deflagrating) qualities at low pressures may promote safety in terms of storability.

From a performance perspective, it is evident from Table 1.1 that the HTPB/LOX system yields the greatest specific impulse of the systems examined, resulting from the significantly higher combustion temperature and slightly lower molecular weight of the combustion products. However, the HC/AP reverse hybrid systems yield greater density specific impulse than the classical hybrid system, primarily due to the high oxidizer density. The HC/AP systems also produce similar performance parameters to the HTPB/AP composite propellant, while maintaining the throttling and stop-start capabilities of a hybrid.

1.3   Objectives

This current study aims to explore the feasibility of and to characterize such a reverse hybrid system that utilizes a solid oxidizer and a gaseous fuel. While AP was selected as an illustrative example of a solid oxidizer for this study due to its high density and stability,

significant research efforts are being devoted to developing and characterizing new "green" solid oxidizers [17, 27, 28]. Gaseous fuel was selected, as opposed to a liquid, such that the focus of the work could be the characterization of the system without the added complexities of liquid injection. Pressurized counterflow experiments were conducted, combusting pressed AP pellets with ethylene (C_2H_4) and methane (CH_4), to examine the pressure, strain rate, and fuel dependencies of the system. This apparatus was also utilized to examine pressure and oxidizer flow rate dependencies of HTPB and GOX. Additionally, static rocket motor firings were conducted to provide insight into the viability of the system as well as exploring the operating parameters of the reverse hybrid.

Chapter 2

Sample Preparation and Considerations

2.1   AP Preparation and Considerations

Solid strands and pellets and center-perforated grains for the current study were pressed at Naval Surface Warfare, Indian Head facilities from 99.8% chemically pure, 200 micron ammonium perchlorate obtained from Kerr-McGee. Table 2.1 provides parameters from the manufacturing process as well as sample measurements and statistics. Images of AP pellets and grains are provided in Figure 2.1.

Table 2.1. Ammonium perchlorate sample preparation parameters.

Sample Type	Length [mm (in.)]	Outer diameter [mm (in.)]	Inner Diameter [mm (in.)]	Density ± σ [g/cm^3]	Pressing Force [kN (ton)]	Dwell Time [s]
Pellets	9.68 (0.381)	10.0 (0.395)	N/A	1.90 ± 0.02	44.5 (5.0)	90
Strands	37.7 (1.48)	9.52 (0.375)	N/A	1.93 ± 0.01	71.2 (8.0)	90
CP Grains	50.8 (2.0)	22.2 (0.875)	9.53 (0.375)	1.88 ± 0.02	106.7 (12.0)	90
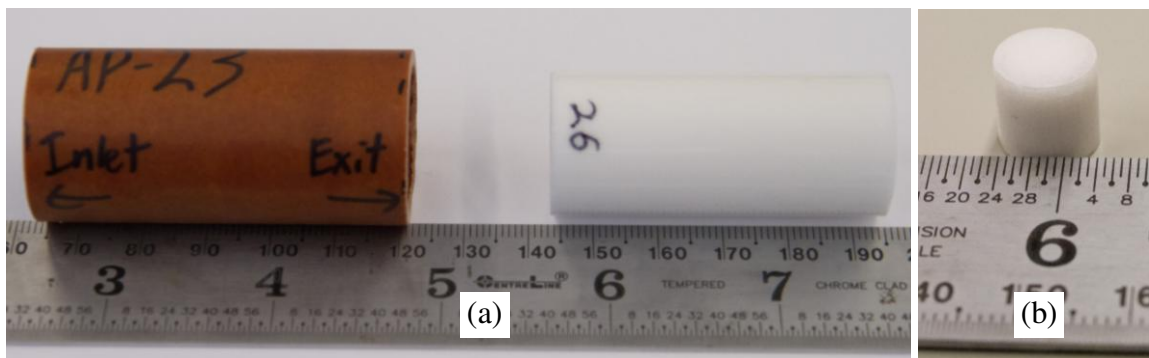
Figure 2.1. Sample images of an AP center-perforated grain with phenolic liner (a) and a pellet for the pressurized counterflow experiment (b).

Ammonium perchlorate is well-known to self deflagrate at pressures above about 2.7 MPa, with either single crystals or pressed pellets [29, 30], so as a means of comparison with the literature, several strands of AP were tested in a strand burner in a nitrogen environment at pressures up to 12.4 MPa. Despite the use of several ignition methods, from a hot nichrome wire to a small piece of composite propellant, the AP used in this study would not self deflagrate, even at high pressures. The cause of this phenomenon is unknown, however it has been postulated to potentially be an effect of impurities, potentially calcium triphosphate, an anti-caking agent [31]. The pressure-dependent burning rates of AP have been examined in a number of studies, using strands [32] and pellets [30, 33] pressed from AP powders, and crystals [29, 30, 34] grown from solution. The deflagration rate of AP is reportedly unaffected by sample type (i.e. crystalline or solid, independent of the nominal particle size), provided that the material is of an ultra-high purity grade and near the theoretical maximum density (TMD) [30, 35]. Boggs *et al*. suggest that the presence of trace impurities in AP may affect the burning rates and may be responsible for ignition difficulties [35].

2.2   Gaseous Fuels

This study utilized both compressed ethylene (C_2H_4, 99.5% chemically pure) and compressed methane (CH_4, 99% chemically pure) to combust with the AP. Ethylene often enters its supercritical regime at conditions found during counterflow tests and rocket motor firings, causing it to deviate from ideal gas behavior. To accurately determine the choked mass flow through the flow-controlling orifices used in this study, calibrations were performed with mass flow meters calibrated for ethylene. This generated a relation for the mass flow as a function of pressure upstream of the orifice, orifice throat area, and orifice discharge coefficient. This procedure was also performed for methane and was found that the methane choked mass flow

rates agreed with ideal gas assumptions since the gas was well above the critical temperature and pressure. Details of these correlations and flow rate calculations can be found in Appendix A.

2.3   HTPB Preparation

The HTPB samples for pressurized opposed flow testing were prepared using R45M hydroxyl-terminated polybutadiene and MDI cross-linking agent. The mixture ratio, by mass, was 1:8.29 MDI to R45M HTPB, resulting in the mass of MDI being about 12.1% of the mass of R45M HTPB. The MDI and HTPB were mixed for ten minutes by hand and then transferred to a vacuum chamber for eight minutes for degassing. The resin was then poured into a mold, which had been coated in PTFE mold release, for eight 0.953 cm (0.375 in.) diameter and 8.89 cm (3.5 in.) long strands and allowed to cure for 48 hours. These strands were then cut to approximately 0.953 cm (0.375 in.) in length and any mold flashing was removed. The average and standard deviation of the measured density of the samples were 0.928 ± 0.012 g/cm^3.
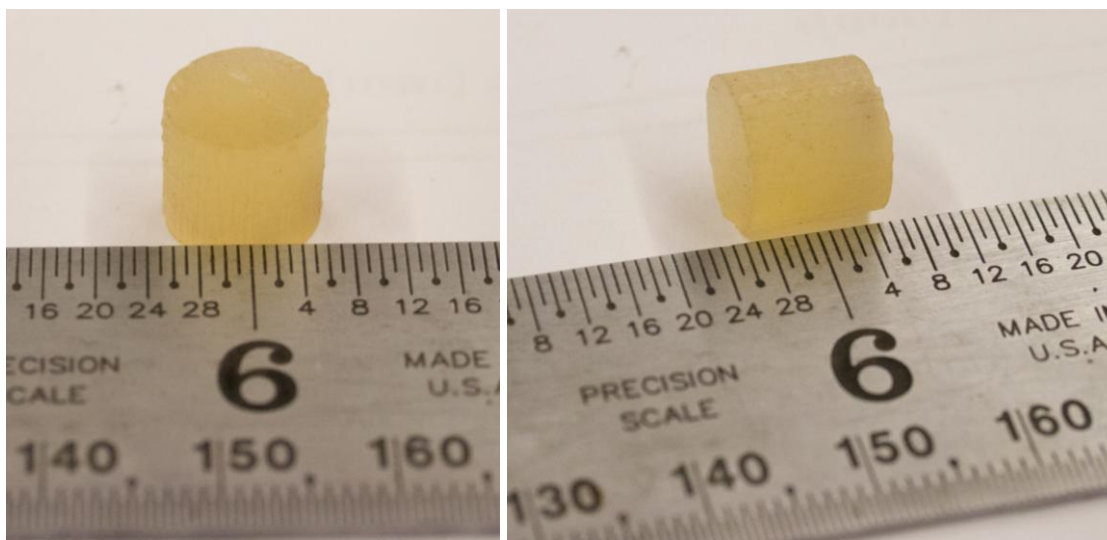
Figure 2.2. Images of an HTPB pellet prepared for the pressurized counterflow experiment.

Chapter 3

Experimental Setup

3.1   Pressurized Opposed Flow Burner

Experiments were conducted in a pressurized counterflow burner to examine the effect of strain rate on the decomposition of a solid oxidizer in the presence of gaseous fuel at elevated pressures, and to attain burning rates for the determination of reverse hybrid motor operating parameters.   Counterflow tests were used to mimic the multidimensional hybrid motor environment with a simple one-dimensional analysis, as depicted in Figure 1.1. Such systems, where gaseous fuel and oxidizer are flowed from opposing, axially aligned, tubes [36] or contoured nozzles [37], are typically employed in an effort to observe and characterize the flame structure occurring near the stagnation plane by controlling the flow rates of the individual reactant constituents.   These systems often employ a co-flow of inert gas surrounding the reactant flows to quench the flame and prevent shear-induced mixing, as the fuel and oxidizer would otherwise be injected into a quiescent environment. Flame strain rates may then be varied by altering the oxidizer and fuel flow velocities or the separation distance between the flow tubes.

Counterflow studies with AP have previously been conducted near atmospheric pressure conditions for fuels simulating the decomposition products of HTPB [38, 39], as well as methane [40] and ethylene [4, 17], where the oxidizer, in the form of a pressed pellet, is fed upwards toward the opposing gaseous fuel flow using a transducer to record the rate of pellet decomposition. These researchers reported that the resulting diffusion flame lay on the oxidizer side of the stagnation plane, and the AP decomposition flame existed between the diffusion

flame and decomposing AP surface [4, 38-40]. For such a system, the following equation may be used to determine the flame strain rate [37]:

$$K = \frac{2(u_O)}{L}\left[1+\left(\frac{u_F}{u_O}\right)\left(\frac{\rho_F}{\rho_O}\right)^{\frac{1}{2}}\right]$$ (1)

The origins of the above equation may be credited to Seshadri and Williams [41], where "K," is the strain rate, in units of inverse time, ρ and u represent the density and velocity magnitude, the subscripts O and F refer to oxidizer and fuel respectively, and "L" is the total separation distance [37]. The oxidizer density and velocity were calculated using conservation of mass, making assumptions of steady state conditions and ideal gas, having a solid AP pellet entering the control volume and AP decomposition products exiting at the surface temperature of 825 K [4]. It is notable that Equation 1 differs from the equation used by Puri and Seshadri [36] by a factor of 2. This is discussed by Chelliah *et al*. and concerns the treatment of flow conditions (i.e., plug versus potential flow), and they suggest that most systems are best described by the former of these two flow conditions [37].

Additionally, counterflow experiments were performed in this study to examine the pressure and strain dependencies of the burning rate of HTPB combusting with GOX. Chemical equilibrium calculations were performed with CEA to determine the average molecular weight of the decomposition products leaving the HTPB surface, omitting condensed phase carbon from the products, yielding an average molecular weight of 42.5 g/mol. This was then used in conjunction with the chamber pressure and a surface decomposition temperature of 1000 K [42] to obtain the fuel density and velocity terms necessary for computing the strain rate, enabling comparison with published HTPB regression rate data at atmospheric pressure. To correlate and compare regression rate data obtained at varied pressures and account for the changes in velocity

and mass flow at elevated pressures, the momentum flux of the oxidizer was computed using Equation (2) for uniform flow across an area, A_{exit}, with $\dot{m}$ being mass flow and $\vec{V}_{avg}$ being the average velocity [43]:

$$\beta = Momentum\ Flux = \frac{\dot{m}\vec{V}_{avg}}{A_{exit}} \tag{2}$$

The experimental apparatus (see Figure 3.1 and Appendix B), utilizes a counterflow burner placed in a windowed pressure vessel, previously used to conduct burning rate tests of solid propellants [44]. The plug in the top plate of the burner was modified (see Appendix B) in order to add gas supply lines and wire feed-throughs, and the entire system was hydrostatically pressure-tested to 10.4 MPa (1,515 psia) prior to conducting any tests. The counterflow burner for this study was designed to hold a 1 cm diameter cylindrical pellet by means of a thin nickel chromium wire, such that the top surface of the pellet would remain parallel and at a fixed distance away from the gaseous component, shown in Figure 3.2. The base of the burner containing the pellet was designed such that half could be removed to load the sample. Both the velocity of the fuel and the separation distance between the pellet and fuel flow tube could be varied between tests in order to vary the strain rate, however for these tests the separation was fixed at 5.0 mm (0.197 in.) and only the fuel velocity was varied. A linear variable displacement transducer (LVDT) was located beneath the pellet, maintaining the separation distance between the decomposing pellet surface and the fuel flow exit, while simultaneously measuring the pellet burning rate with an accuracy of 0.25%. The surface of the pellet was typically located 1.25 mm (0.049 in.) from the top of the pellet holder using stainless steel pins, which offset the retaining wire and prevented the pellet holder from behaving as a heat sink near the decomposing region of the sample. The burner was also designed to be operated with co-flows of an inert gas around

Number	Description
1	Compressed Fuel
2	Compressed Argon
3	Two-stage Pressure Regulator
4	Electro-pneumatic Solenoid Valve
5	Setra Pressure Transducer
6	Fuel Orifice
7	Fuel Co-flow Orifice
8	Oxidizer Co-flow Orifice
9	Linear Variable Displacement Transducer
10	Teflon Spacer
11	Oxidizer Pellet
12	Pressure Vessel
13	Exhaust Valve
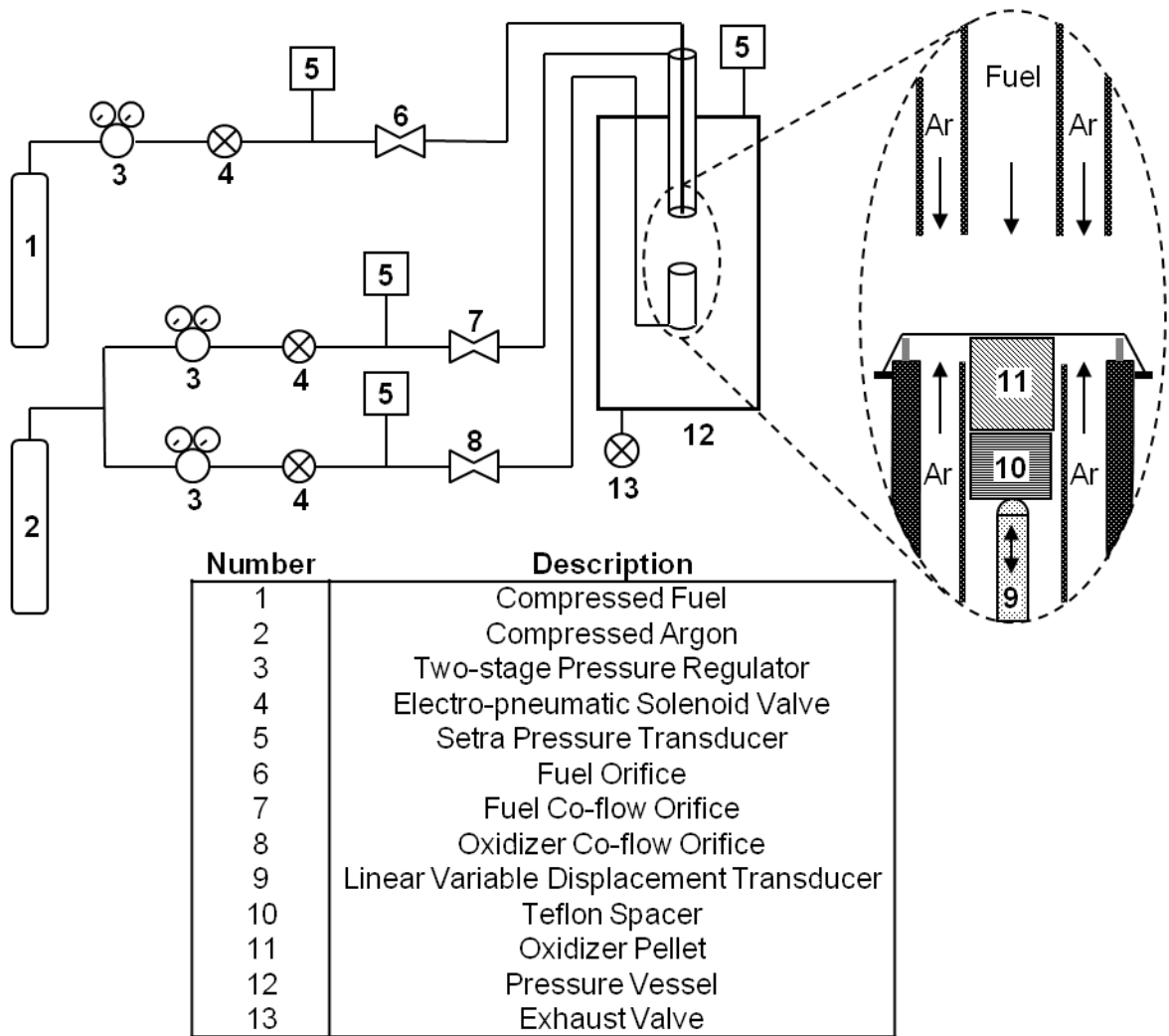
Figure 3.1. Block diagram of counterflow burner used in current study.
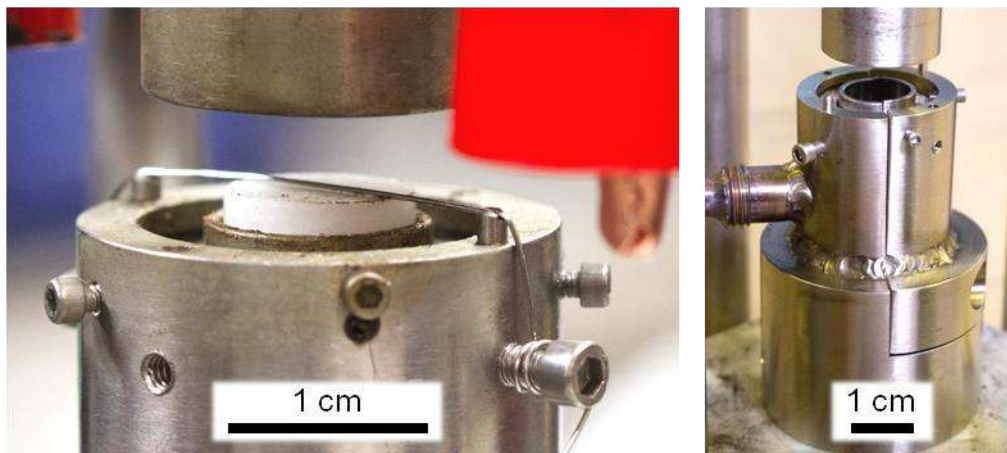
Figure 3.2. Images of pellet holder base for pressurized counterflow burner.

both the fuel and oxidizer to aid in quenching the flame and isolating the reactants during the test. The inner diameters of the concentric fuel and fuel co-flow tubes were 0.775 cm (0.305 in.) and 1.575 cm (0.620 in.), respectively. The oxidizer co-flow, having an inner diameter of 1.204 cm (0.474 in.) and an outer diameter of 1.905 cm (0.750 in.), flowed into a duct that was machined into the pellet holder and then passed through a stainless steel sintered ring that equalized the flow around the sample.

The flows of the fuel and co-flow gases into the chamber were controlled with electro-pneumatic solenoid valves and choked flow orifices. Before each counterflow test, the pressure upstream of each valve was set, using pressure regulators, based on the calculated pressure required to achieve a certain exit velocity for a given orifice size and discharge coefficient, gas type, and exit area (see Appendix A). The orifices were chosen such that the velocity of the co-flow would approximate the velocity of the fuel or oxidizer. Calibrated Setra pressure transducers (with uncertainties of $\pm$ 0.13% of full scale) monitored pressures upstream of each orifice and within the pressure vessel, allowing the determination of gas flow rates into the chamber and the monitoring of chamber pressure. The pressure transducer and LVDT signals were recorded using a Nicolet Genesis data acquisition system having a sampling rate of 250 Hz. The solenoid valves employed to initiate and shut off fuel and co-flow gas flow into the chamber and the igniter were controlled remotely using a custom LabView control sequencing program and external relay board.

Ignition of the pellet was achieved using a nichrome wire placed on the surface of the pellet. Resistive heating of the wire was accomplished via igniter leads that passed through high pressure feed-throughs at the top of the chamber. Prior to testing, a purge cycle was employed to remove entrapped air by pressurizing the chamber with argon then exhausting the gases from the

15

volume. The chamber was then pressurized using argon, fuel flow was initiated, and the system was allowed to equilibrate while the chamber exhaust was metered to maintain a nearly constant pressure environment, at which point the pellet was ignited using the nichrome igniter. During the test, separation distance and flame visualization were recorded using a standard digital video camera located at one of the chamber optical ports. After the completion of the burn, the chamber was depressurized and purged with argon to remove the remaining combustion products.
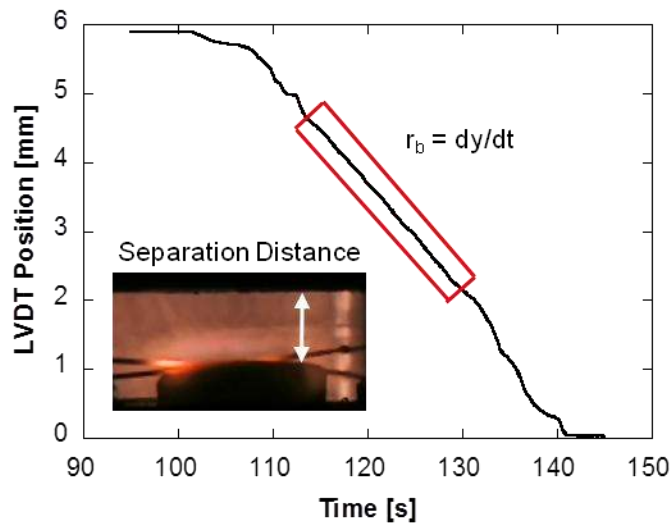
Figure 3.3. Sample burning rate determination from LVDT trace and separation distance determination from video footage.

Analysis of video footage indicated that following ignition, the separation distance between the pellet surface and fuel exit was slightly reduced as a result of the formation of a melt layer on the pellet surface and the thermal expansion of the retaining wire. As a result, the separation distance varied on a test to test basis, typically falling between 3.5 and 4.5 mm, and it was these measured values that were used in the data reduction process. The burning rate of the pellet was obtained from the LVDT profile after any ignition transient had passed, while the

16

separation distance during this time period was determined from the video, as shown in Figure 3.3. The velocities of the fuel and co-flows at the tube exits during the test were then calculated from recorded upstream and chamber pressure data. These data, along with the burning rate data recorded from the LVDT, were then used to calculate the flame strain rate (Equation 1).

3.2   Hybrid Rocket Motor

The lab-scale motor, used in the current study to characterize the viability of the reverse hybrid system, was previously developed and characterized using gaseous oxygen (GOX) as the oxidizer with polymethyl methacrylate (PMMA) and HTPB as solid fuels [45]. The combustion chamber is 30.5 cm (12 in.) long and has an inner diameter of 2.79 cm (1.1 in.), with further detail being provided in reference [45]. Method of grain manufacture and system setup for the current study are described in the following paragraphs. Modified schematic drawings of the hybrid rocket motor as operated in these experiments are provided in Figure 3.4 and Figure 3.5. The motor was instrumented with calibrated Setra pressure transducers (with uncertainties of $\pm$ 0.13% of full scale) recording both the pre- and post-combustion chamber pressures, in addition to a load cell (with an uncertainty of $\pm$ 0.56 N [0.12 lb]) for measuring thrust generated by the motor. Center-perforated AP grains, about 5.3 cm (2.1 in.), were tightly fit into a paper phenolic tube liner that provided a barrier between the combustion chamber and hot combustion products and may permit stacking of several AP grains, allowing the formation of a segmented grain structure. Nozzles used in the motor had a simple conical converging/diverging design with an area expansion ratio of 5 and were machined from high-density graphite.
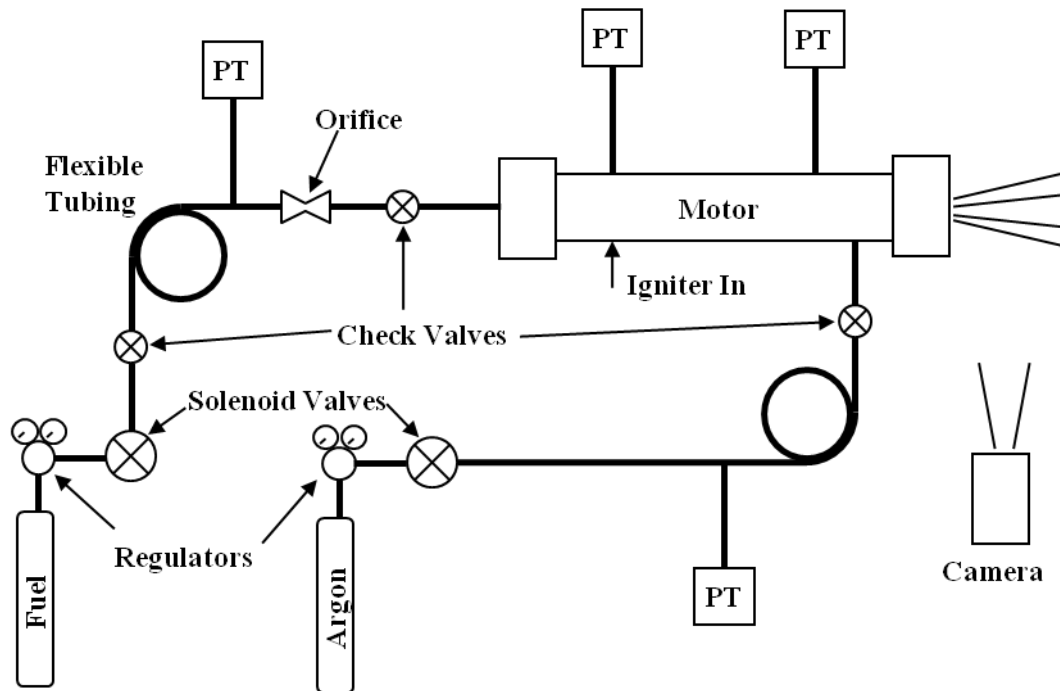
Figure 3.4. Block diagram of pre-pressurized hybrid rocket motor system.
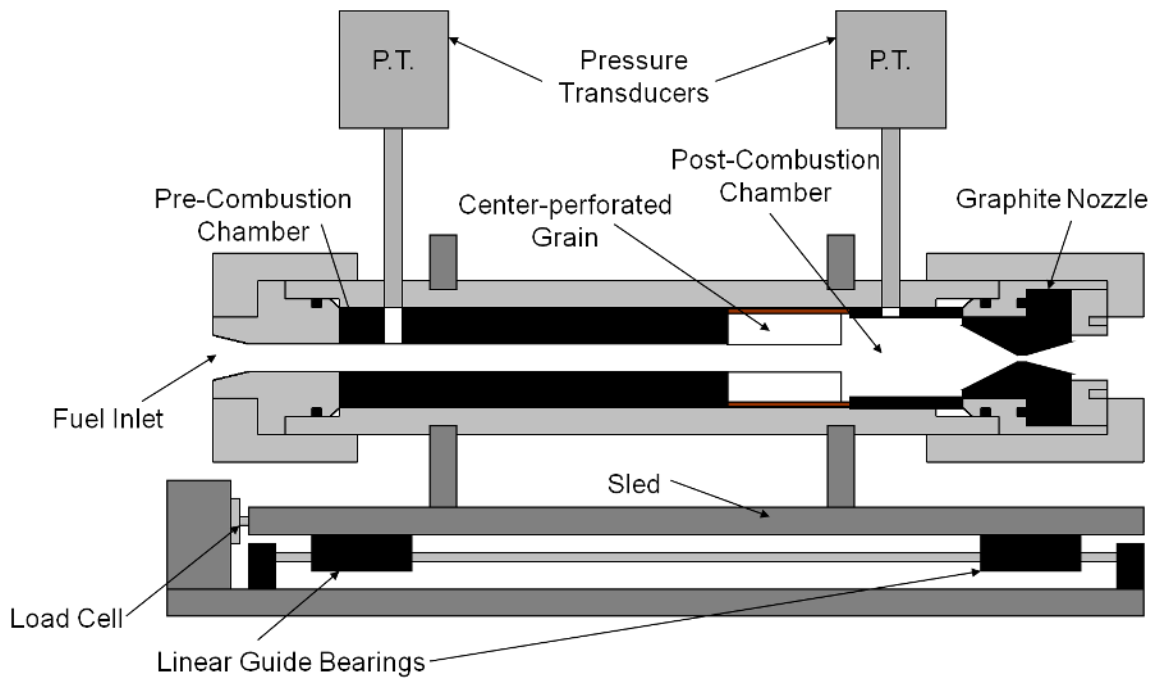
Figure 3.5. Detailed schematic of rocket motor set up for reverse hybrid operation.

The simple model presented by Connell *et al.* [45], which couples conservation of mass, assumptions of ideal gas and equilibrium reactions with empirically-determined burning rates and properties of the oxidizer and fuel, was modified for the current system to aid in the determination of motor operating parameters and the development of a tentative motor test matrix. Pressurized opposed flow data from this study were used to determine the burning rate as a function of pressure for target nozzle dimensions and fuel flow rates. The model suggests under low pressures the inverse system may operate much like a gas generator, the grain being consumed without yielding any performance gain. However, given the proper initial conditions, the system shifts into a progressive burn much like that of a composite propellant. This suggests the combustion process will be strongly dependent on the initial motor conditions and ignition process. Decoupling ignition from the combustion process would require some form of system pre-pressurant or a high fuel mass flow rate to initially boost chamber pressure, and bypass a significant ignition delay. Although a high fuel flow rate may be sufficient to bypass the low-pressure region and transition the combustion process to the second regime, it would not be advantageous from the perspective of fuel conservation. As such, the igniter should supply the pre-pressurant necessary to transition the system into the higher pressure regimes in addition to fully and reliably igniting the grain.

Several methods of ignition were considered for the current system, with a piece of M9 (double-base) gun propellant ignited with a hot nichrome wire being selected based on simplicity and reliability. The nichrome/M9 igniter was placed within the grain port inlet during motor assembly, the electrical leads passing through an electrical feed-through located in the pre-combustion chamber. To accommodate motor pre-pressurization, inert argon gas was flowed into the post-combustion chamber providing sufficient mass flow to achieve the desired pressure.

The gas flow control system, similar to the system developed for the pressurized counterflow burner, employed electro-pneumatic solenoid-driven ball valves to cycle the gases, and choked orifices to meter the flow into the injection head end of the motor. Inline check valves prevent reverse pressurization of the supply lines in the event of motor overpressurization. Calibrated Setra pressure transducers placed upstream of the orifices were used to record pressures and aid in determination of mass flow rates. The firing sequence was controlled using
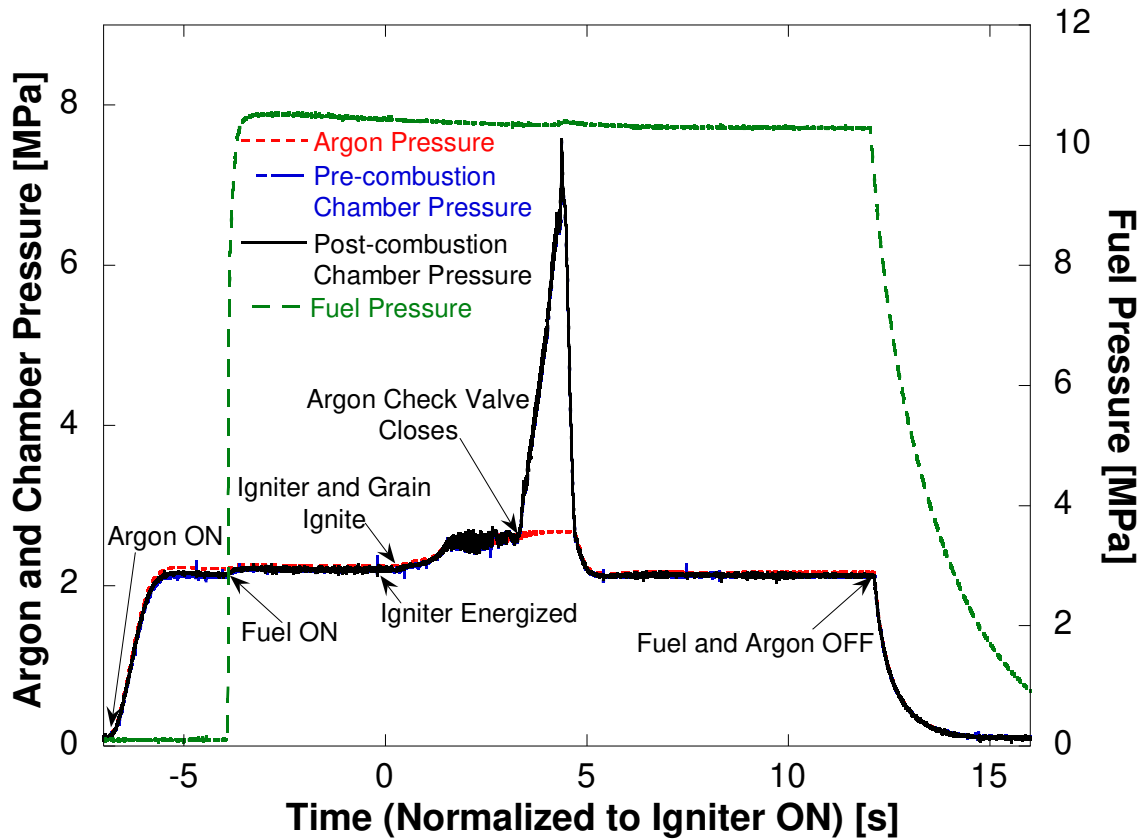
Figure 3.6. Typical pressure-time profiles from a typical reverse hybrid motor experiment.

a custom time-based LabView program and external relay board. The signals from the chamber and orifice pressure transducers, the load cell, and an igniter trigger signal were all recorded with a Nicolet Genesis data acquisition system at a sampling rate of 1,000 Hz. An example of data recorded from a typical firing is provided in Figure 3.6 and Figure 3.7, with the run-time events

indicated on the plots. To initiate the run, the system was purged with argon to prevent a premixed fuel-air condition prior to ignition, after which the pre-pressurant flow was initiated. The fuel solenoid valve was then cycled open, permitting gaseous fuel to flow through and be exhausted from the motor. After sufficiently purging the pre-combustion chamber and grain port with fuel, the igniter system was fired, igniting the oxidizer grain that was then combusted with the injected fuel. Inline regulators, check valves, and Setra pressure transducers limited and measured the argon line pressure, such that increasing chamber pressures shut-off the argon pre-
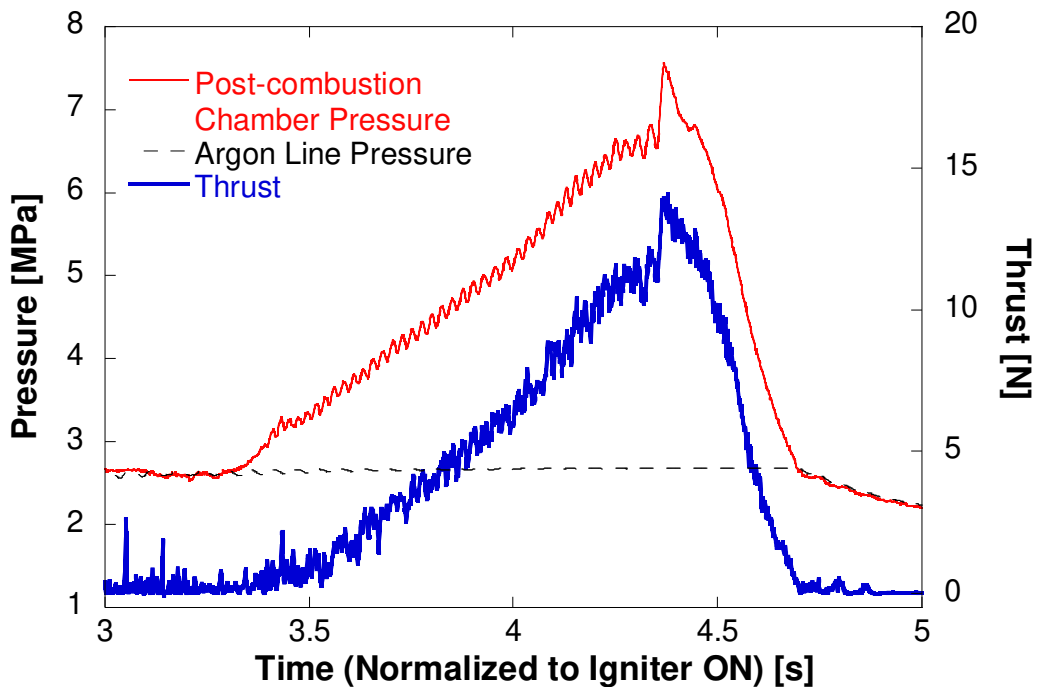
Figure 3.7. Details of pressure and thrust from a typical reverse hybrid motor experiment.

pressurant flow into the motor, which was then verified through recorded argon line pressure data. Upon completion of the run, the fuel and pre-pressurant gases were shutoff via solenoid valves. The cartridge and any remaining grain were then removed from the chamber for analysis.

Chapter 4

Discussion of Results

4.1 Pressurized Counterflow Experiment Characterization

The counterflow burner was characterized using pellets of HTPB with gaseous oxygen impinged on the surface, comparing the results with experiments performed by Risha *et al*. [46] (Figure 4.1) at atmospheric pressure. Both this characterization study and the work by Risha *et al*. were performed without inert co-flows around the oxidizer flow or pellet sample. The comparison indicates that this experiment correlates well with existing data, generating confidence in the results obtained with this apparatus. The combustion of HTPB is governed by a diffusion flame between the fuel decomposition products and the impinging oxidizer, resulting in a dependency of the regression rate on the flame strain rate.
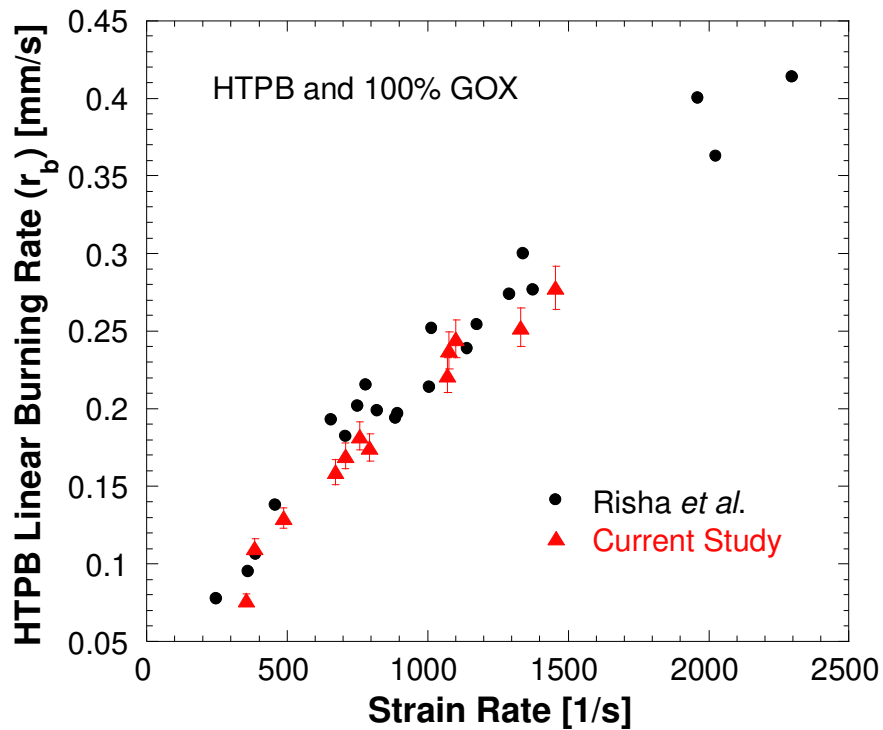
Figure 4.1. Counterflow apparatus characterization comparing HTPB regression rate at

atmospheric pressure as a function of flame strain rate with published data [46].

After verifying the functionality of the apparatus, experiments were performed at varied pressures to examine the dependence of HTPB regression rate on pressure and strain rate. Hybrid fuel regression rates are typically correlated as functions of oxidizer mass flux or velocity, and this works well at a constant pressure. When comparing different pressures, however, it becomes necessary to take into account the effect of changes in density and how it affects velocity and mass flow rates. From this understanding, the regression rates obtained in this study at different pressures were correlated as functions of momentum flow rate as described in Equation (2). Figure 4.2 displays these results for pressures ranging from atmospheric up to 4.32 MPa (626psia), indicating that the regression rates are not pressure dependent.

Figure 4.2. Regression rate of HTPB at various pressures as a function of momentum flow rate, compared with published data [46].

Figure 4.3. Analysis of pressure dependence on HTPB regression rate at a fixed momentum flux.

To further examine the pressure dependence of the regression rate, a series of experiments were performed which targeted a fixed momentum flow rate while varying chamber pressure. The results of this analysis are provided in Figure 4.3 and indicate that the regression rate has no dependence on pressure. This result is expected for a diffusion flame-controlled system, as the flame is limited by the diffusion of reactants into the flame zone [47]. The data at 1.55 MPa and 2.91 MPa are believed to have higher regression rates due to reduced separation distances between the pellet and the oxygen flow tube during the test. This results in an increase in the flame strain rate, which Figure 4.1 shows can increase the regression rate. Error for these counterflow analyses was determined from the average and standard deviation of several repeat tests at atmospheric pressure showing the repeatability of the system.

4.2   Pressurized Counterflow Experiments with AP/Fuel

The results from the counterflow burner experiments with AP/fuel for all flow conditions tested are detailed in Figure 4.4, which displays the pressure effect on burning rate, demonstrating a burning rate transition around 1 MPa and a second transition around 3 MPa. These transitions are the result of the flame structure of AP combusting in the presence of a fuel, described by Beckstead *et al.*, having two flames: a monopropellant flame from the AP decomposition, and a diffusion flame where the monopropellant flame products are combusted
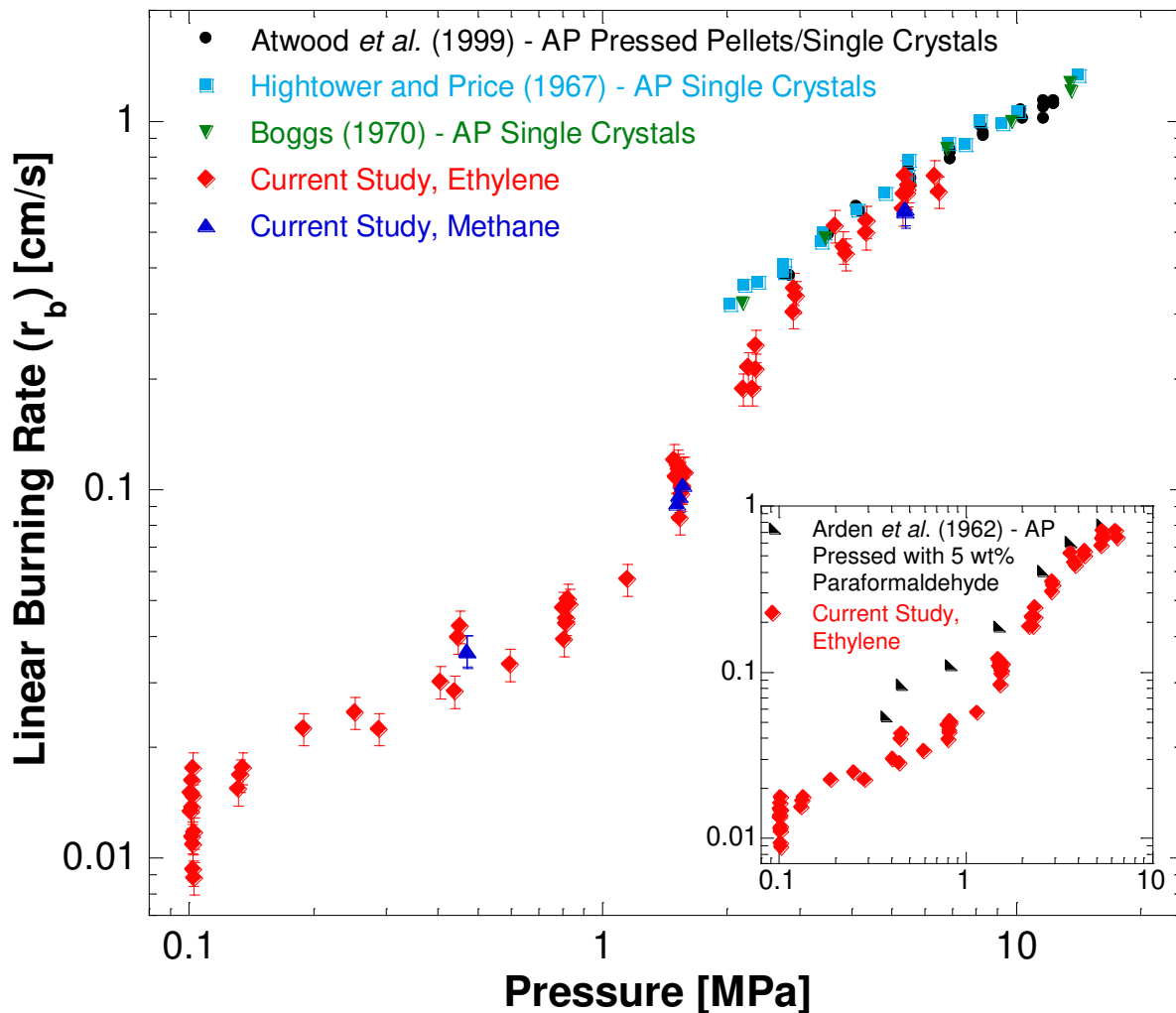
Figure 4.4. Counterflow burning rates as a function of pressure, compared to published data [29, 30, 34, 48]

with fuel [49]. Under atmospheric conditions well below the AP self-decomposition pressure, the presence of the monopropellant flame has been observed by researchers in counterflow experiments [4, 39]. This is due to the presence of the AP/fuel diffusion flame that reduces heat loss downstream from the AP decomposition flame, enabling a sustained reaction or, depending on the proximity of the diffusion flame to the AP surface, providing additional heat to the surface by increasing the surface temperature gradients, thus increasing the AP decomposition rate [32, 49, 50]. Considering the monopropellant flame, Glassman and Yetter show that for a reaction order of two, reaction rate scales linearly with pressure, thus the chemical reactions in the AP
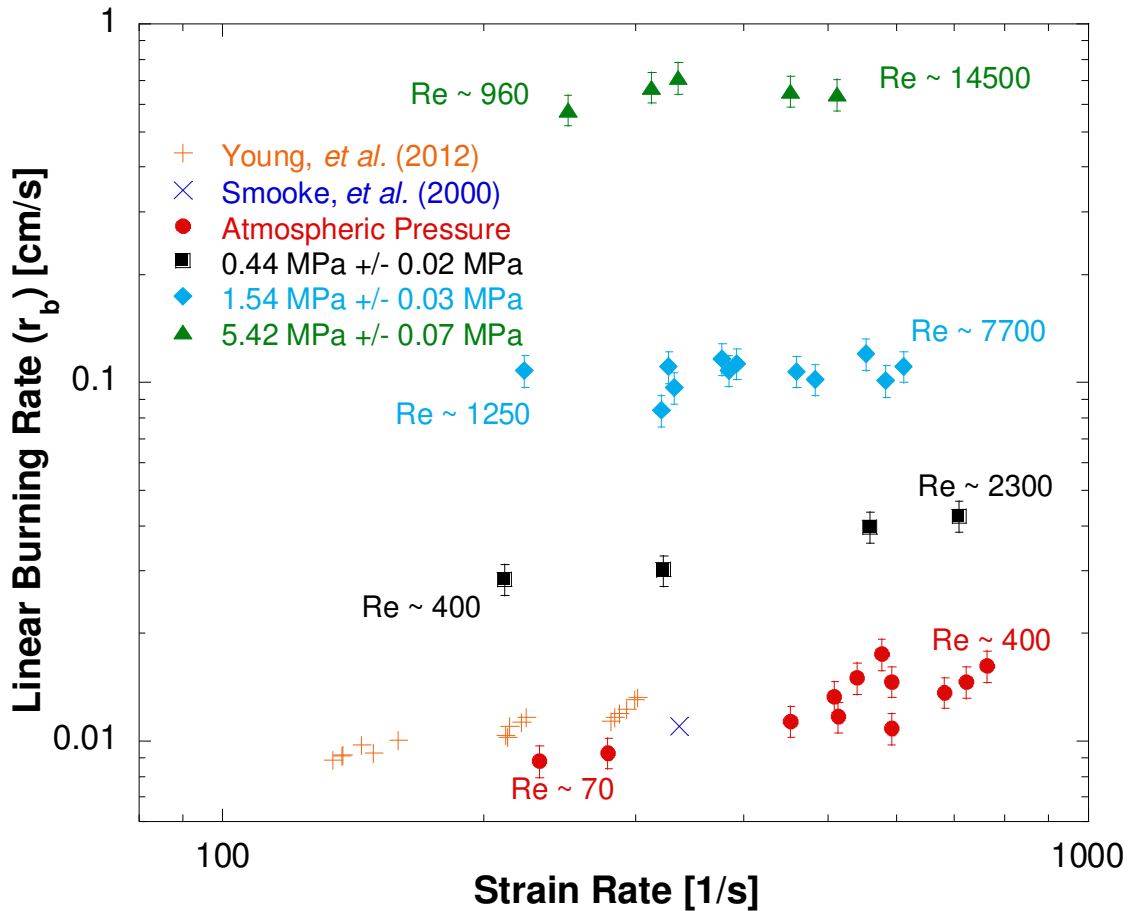
Figure 4.5. Dependence of burning rate on flame strain rate and pressure for AP and ethylene, compared to published data [4, 17].

monopropellant flame occur faster with increasing pressure, shifting the monopropellant flame closer to the surface without changing the position of the diffusion flame and increasing the heat feedback to the AP surface. At high pressures, despite the presence of the diffusion flame, the measured AP burning rates transition and correspond well with published literature [29, 30, 34], suggesting AP decomposition is controlled by the monopropellant flame. The dominance of the monopropellant flame at high pressure is in agreement with the Beckstead, Derr and Price (BDP) model of AP combustion with fuel [49]; however, while it does not control the combustion process, the thermal energy from the diffusion flame reduces the heat loss from the monopropellant flame, as strand tests attempted for the current study were not successful. Error in the experimental results was computed by examining the average and standard deviation of several data points at nearly identical pressures.

These results are further supported by examining the burning rate of the AP with ethylene as a function of pressure and strain rate, as presented in Figure 4.5. During testing, as pressure and fuel flow velocity were increased, the flame structure above the pellet was observed to shift from laminar to turbulent. This observation was confirmed through determination of Reynolds numbers (Re) indicated on Figure 4.5. This transition does not appear to have a significant effect on the burning rates. The data at atmospheric pressure from this study show trends similar to the results published by Smooke *et al.* [4] and Young *et al.* [17] at comparable strain rates, with the burning rate exhibiting a weak dependency on the strain rate. As pressure increases, the effect of strain rate on the AP burning rate diminishes, resulting in the burning rate becoming nearly independent of strain rate in the higher pressure burning regimes above 1 MPa. At pressures of 0.1 and 0.34 MPa, increasing the strain rate by 200% affects an increase in burning rate on the order of 40%, while the same change in strain rate produces a change in burning rate of around

27

7% for the 1.38 and 5.17 MPa cases. This behavior is attributed to the interaction of the diffusion flame and the monopropellant flame. At high pressures the diffusion flame is decoupled from the monopropellant flame, essentially maintaining adiabatic conditions between the monopropellant flame and the diffusion flame. Increasing the flame strain rate (i.e., the fuel flow velocity) moves the diffusion flame closer to the AP surface, however at high pressures and for the strain rates considered, the diffusion flame never moves close enough to the AP decomposition flame to affect the surface temperature gradient. Hence there is no effect of fuel flow velocity on the AP burning rate at high pressures. At low pressures, where the AP decomposition kinetics are much slower, the decomposition flame and diffusion flame are much more coupled spatially. Increasing the fuel flow velocity pushes the diffusion flame further into the decomposition flame allowing the temperature gradient to increase slightly, increasing the AP burning rate at the highest flow velocities and lowest pressures, as shown in Figure 4.5. At even higher flow rates, it may be anticipated that the residence times in the flame become too short to sustain the diffusion flame, and both flames would extinguish; however, these conditions were not observed here for the strain rates investigated.

The present results are also significant with regards to the interpretation of the AP solid composite flame structure, as the counterflow geometry essentially represents an infinite AP particle diameter, where the primary diffusion flames of the BDP model for AP composites [49] do not exist. Thus, at low pressures, the structure transitions from a premixed flame limit for very small AP particle diameters to a diffusion flame limit for extremely large AP particle diameters. At high pressure, the importance of AP particle size on the burning rate should diminish, with the limiting cases transitioning between the monopropellant flame limit for large AP particle diameters, the primary diffusion flame limit, and the premixed flame limit for small

AP particle diameters as predicted by the BDP model. The results from Arden *et al*. [48], shown in Figure 4.4, also support this particle size dependence, as their pressed mixture effectively behaves as smaller AP particles, thus they burn faster at lower pressures, while retaining similar burning rates to pure AP samples at high pressure.

4.3   Initial Rocket Motor Experiments

Preliminary experiments with the reverse hybrid rocket motor system examined several methods for igniting the motor. These methods included a coaxial injector, a small commercially available rocket motor, and a piece of double-base gun propellant located at the forward end of the AP grain. While all three systems were capable of igniting the motor, weighing the advantages and disadvantages of each method allowed the selection of the final ignition system.

The coaxial injector technique utilized two concentric tubes, with gaseous oxygen flowing through the central tube and gaseous fuel being flowed through the outer tube. Ignition of the injector was attempted through the use of a resistively-heated nichrome wire at the exit of the tubes, but convective cooling caused this technique to be unreliable. In order to alleviate this inconsistency, the nichrome wire was replaced with an electric match that provided much more reliable, consistent ignition of the injector. The injector provided successful ignition of the grain with the fuel/oxygen diffusion flame, however the method had several drawbacks, including implementation complexity and sensitivity to motor operating conditions. In order to prevent long bleed-down times of the oxygen caused by the small orifices, many electro-pneumatic valves were required, resulting in a very complex ignition system. This method was also sensitive to changes in injector flow velocities and oxidizer-to-fuel velocity ratios, which were controlled by the motor operating pressures and the mass flows through the controlling orifices.

As such, this ignition technique necessitated significant characterization tests to understand and predict its behavior during motor tests.

A second ignition method considered was the use of a small commercially available rocket motor fired into the reverse hybrid motor. This approach provided a simple ignition mechanism that would briefly increase chamber pressure and fire hot combustion products through the AP grain. Two configurations for this igniter were examined: injecting fuel axially into the motor while firing the igniter perpendicularly into the pre-combustion chamber, and firing the igniter axially through the motor while injecting the fuel perpendicularly into the pre-combustion chamber. This ignition process was capable of igniting the AP grain, though it had a couple drawbacks. When firing the motor perpendicularly to the pre-combustion chamber, heat loss to the graphite resulted in cooler gases flowing through the grain and therefore a reduced effectiveness of the igniter. Additionally, this technique often did not sustain the chamber at the desired high pressures for long enough to allow the motor to maintain the chamber pressure after the igniter extinguished.

The third ignition system considered utilized a small piece of M9 double-base gun propellant on a length of nichrome wire that was located at the forward end of the AP grain. Electrical leads were passed through feed-throughs in the pre-combustion chamber to allow resistive heating of the nichrome wire and therefore ignition of the M9. This method improved the reliability of the ignition system, reduced the complexity, and eliminated the heat loss associated with the rocket motor igniters. In order to provide sufficient pressure to the combustion chamber, the M9 was coupled with an argon pre-pressurant system described in the following section.

4.4   Rocket Motor Firings

Static-fired motor experiments were conducted to determine the viability and operational requirements of the reverse hybrid system. These tests varied conditions such as ignition method, fuel mass flow rate, fuel type (ethylene or, when higher delivery pressures were required, methane), and chamber pressure through the use of an inert pre-pressurant. Images of a pre- and post-fired (partially consumed) grain are provided in Figure 4.6. All three ignition methods tested successfully ignited the motor, however they could not generate sufficiently high pressures necessary for the motor to burn in the high pressure burning regimes. As a means of decoupling ignition and pre-pressurization, argon was flowed into the post-combustion chamber to generate the desired initial pressure conditions, and the flow was shut-off during self-sustained operation via an inline check valve.
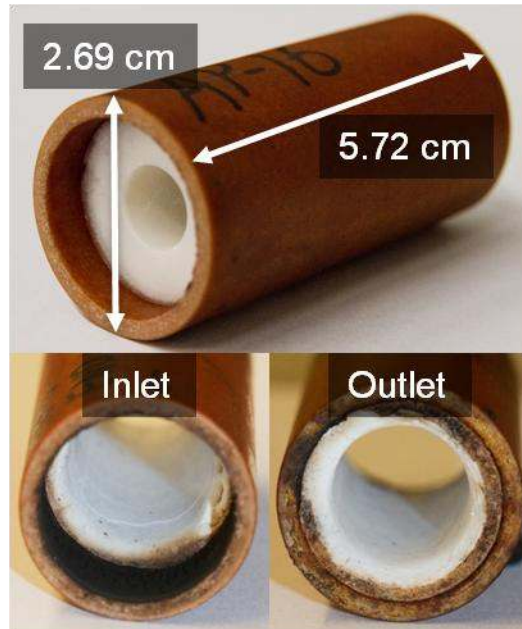
Figure 4.6. Images of an AP grain, before and after firing.
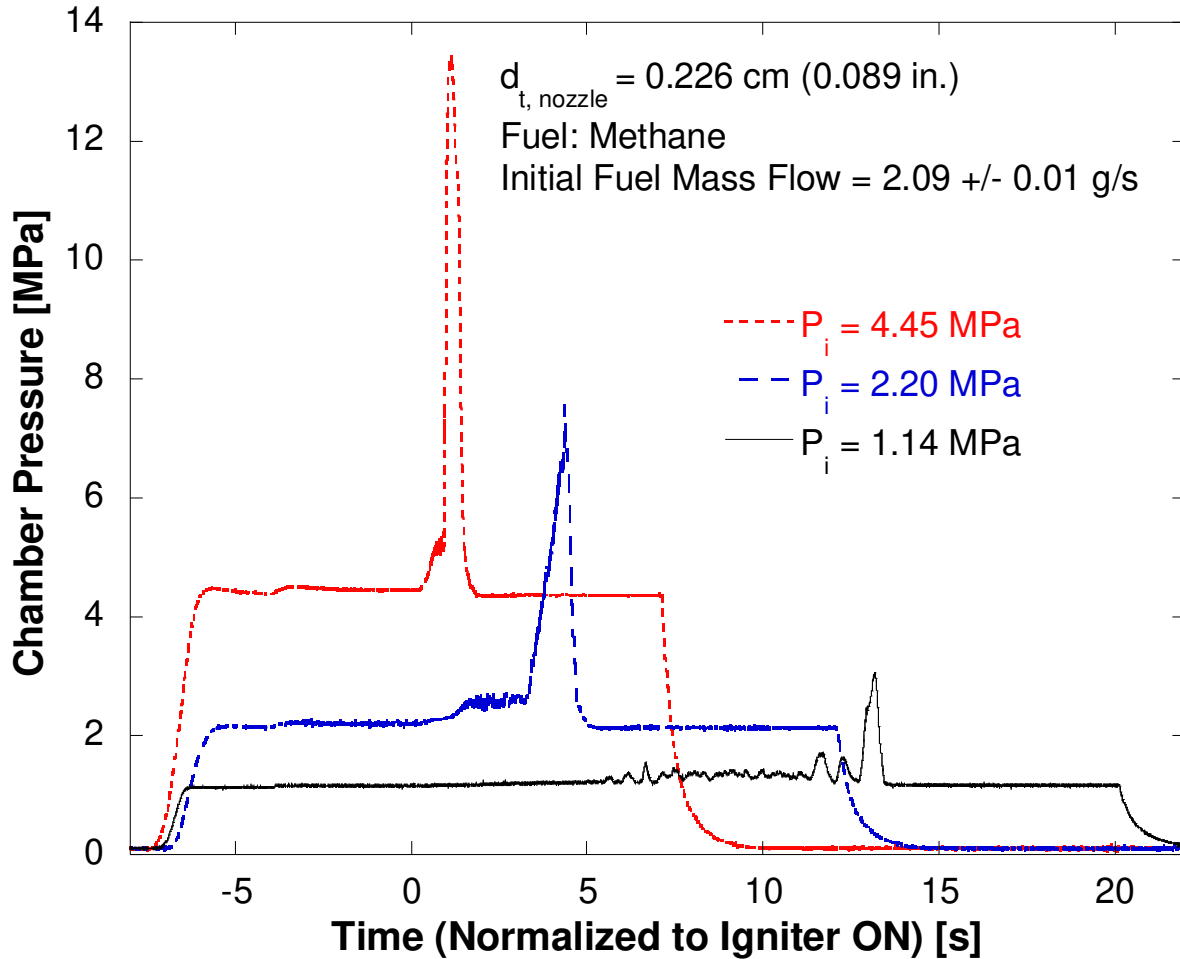
Figure 4.7. Effect of initial chamber pressure on reverse hybrid operating conditions.

The effect of initial system pressure on motor operation was examined by variation of pre-pressurant mass flow into the post-combustion chamber, prior to motor ignition (Figure 4.7). In all cases, the argon pre-pressurant flow was shut off during the firings, as chamber pressures exceeded the argon line pressure. The variations in the initial pressurization time are due to manual opening of the pre-pressurant valve to prevent potentially damaging the grain. Motor results show that low initial pressures are disadvantageous, as a significant portion of the oxidizer mass is consumed in the long startup delay before the system can supply the mass flow necessary to shift to a high pressure burning regime. Pre-pressurizing the system to conditions

well within the middle burning regime yields reduced ignition and startup delays and transitions the system to favorable operating conditions. During several of these runs, the chamber pressure exceeded the choked-flow limit near burnout, reducing the fuel mass flow rate, or in the case of the high initial pressurant, completely shutting off the fuel for approximately 375 ms during peak motor pressure.

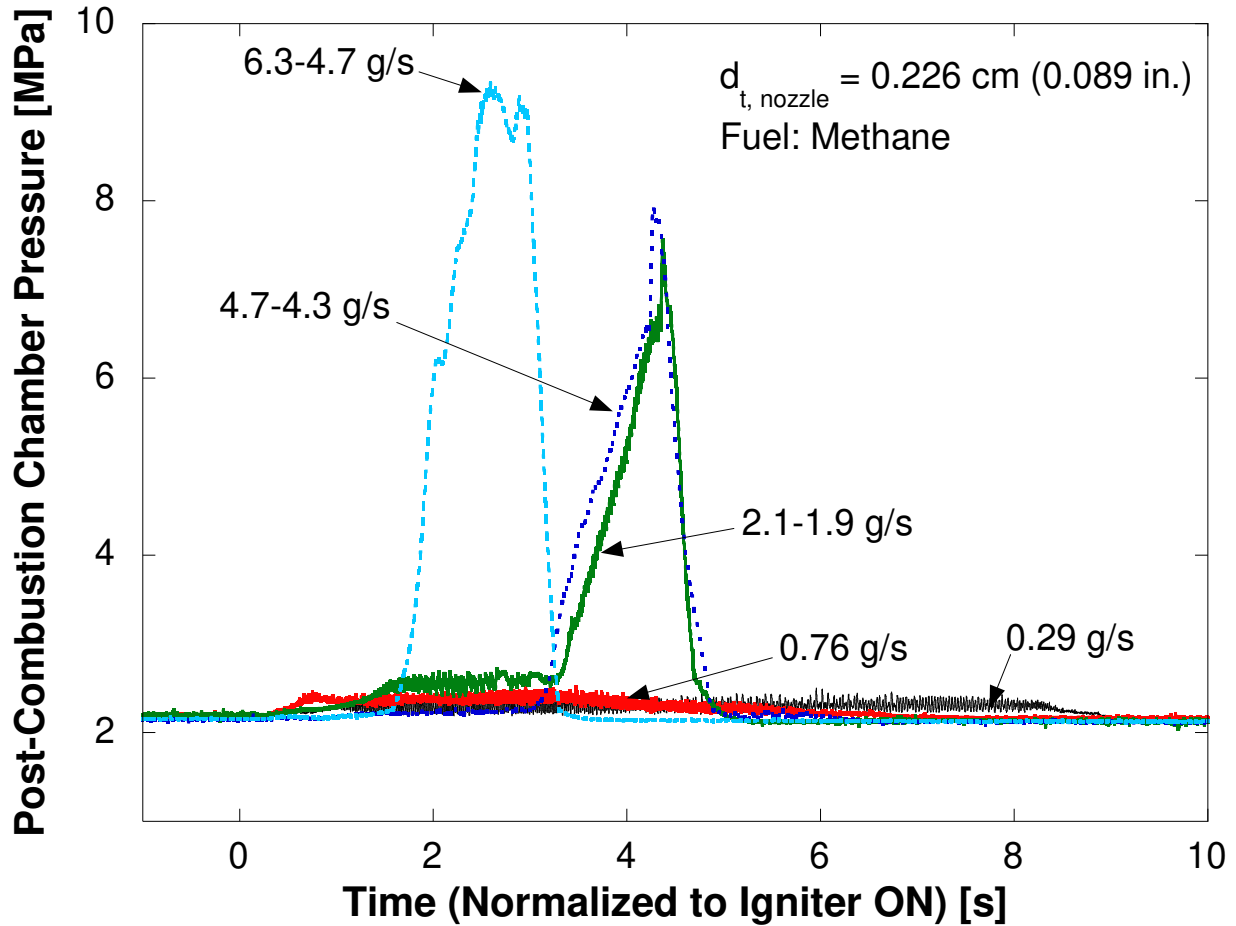Figure 4.8. Effect of fuel flow rate on chamber pressure profiles during reverse hybrid operation, with methane flow rates indicated on plot.

Lab-scale rocket motor experiments were also performed to examine the fuel flow dependency of the system. These tests used a single AP grain and held the initial chamber pressure, nozzle throat, and fuel supply pressure constant, while varying the size of the fuel

orifice to affect a change in fuel flow rate. The results, provided in Figure 4.8, indicate that there is a lower limit on the amount of fuel required by the system to operate in the high burning rate regimes. For fuel flow rates below this limit, the motor behaves as a gas generator, consuming the AP while maintaining the chamber pressure at the pre-pressurant pressure. Above this limit, the chamber pressure profiles during the self-sustained burn are similar, indicating an independence of fuel flow rate. This result is supported by high pressure non-self-deflagrating strand tests that suggest a dependence on the presence of fuel (i.e. heat transfer from the resulting diffusion flame) to sustain combustion.

To examine the regression and combustion characteristics within the reverse hybrid motor, a static firing was conducted having a bored-out nozzle with a 1.746 cm (0.6875 in.) diameter throat, an ethylene flow rate of 0.04 g/s, and a chamber pressure of 0.1 MPa. A mirror placed downstream of the nozzle permitted observation and video recording of the ignition and combustion process as shown in Figure 4.9. Due to the small orifice throat area, a long period of fuel mass flow decay was observed following the valve shut-off, during which the grain continued to burn until all of the AP was consumed. Analysis of the video showed a flame in the core of the motor, with the AP grain bubbling and visibly regressing radially approximately 13 seconds after the igniter was turned on. This delay in apparent regression is likely due to flame spreading across the burn surface. Early in the experiment, a sooty flame is visible at the exit of the motor in addition to the luminous flame in the core of the grain. The calculated bulk equivalence ratio indicates that early in the test the motor is burning under fuel rich conditions, with the stoichiometric AP/ethylene flame being obscured by the ethylene-air diffusion flame at the exit. As the fuel flow rate decreases, the sooty flame diminishes, signifying a shift to a near

bulk stoichiometric condition, reaching a minimum equivalence ratio of 0.97 near 56 seconds into the burn.
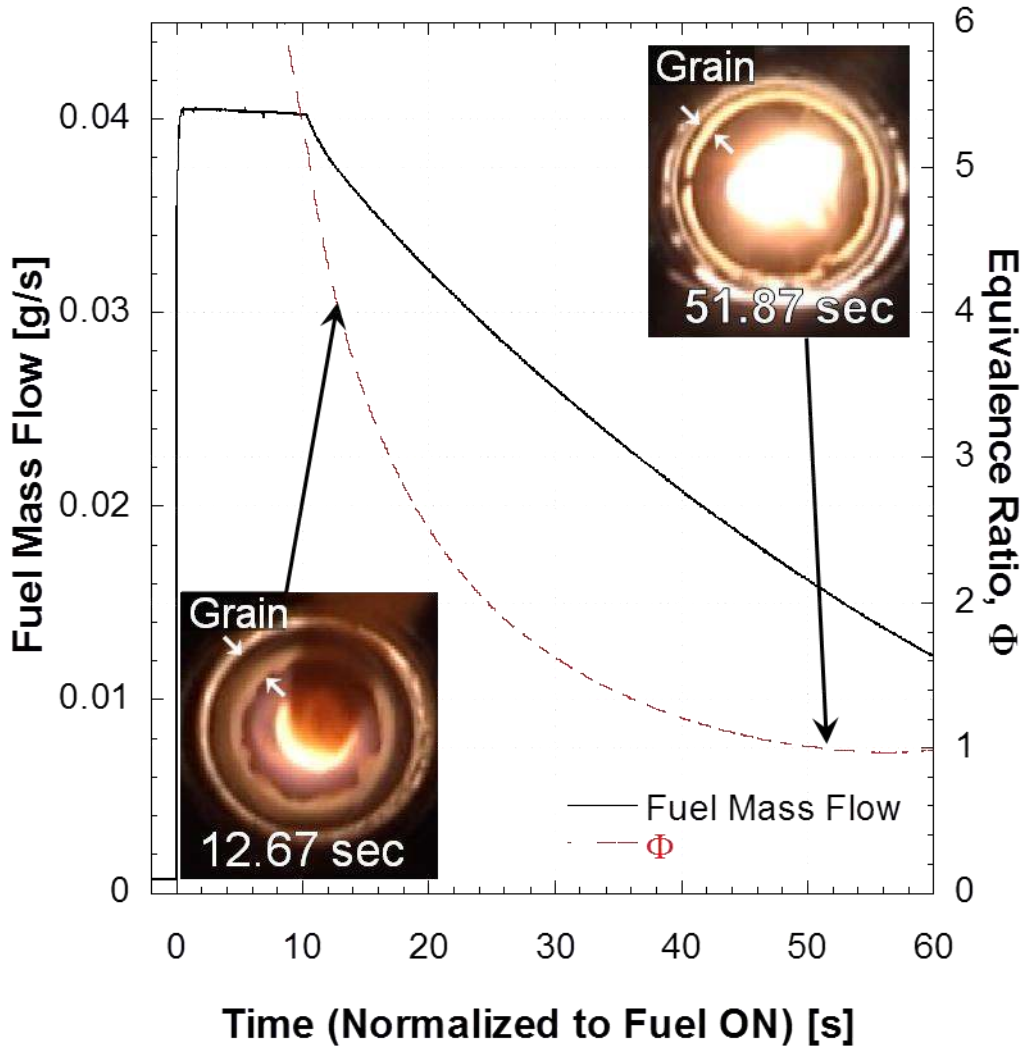
Figure 4.9. Burning grain images and calculated equivalence ratio for center-perforated AP grain burning with ethylene in a reverse hybrid motor at atmospheric pressure.

Examining the elevated pressure counterflow results for AP and gaseous fuel and comparing them with the classical hybrid behavior shows some distinct differences. In a classical hybrid rocket motor, the regression rate of the solid fuel is independent of the chamber pressure due to the diffusion-controlled combustion process. By comparison, the burning rate of

the solid oxidizer in the reverse hybrid system is highly dependent on pressure due to the monopropellant flame above the oxidizer surface. Additionally, at low pressures, the diffusion flame from the combustion of the fuel and monopropellant products generates a slight dependence of the system on fuel flow rate into the motor. In contrast, the fuel regression rate in a classical hybrid is highly driven by the momentum flow rate of the oxidizer into the chamber. Comparing the atmospheric pressure burning rates of HTPB in Figure 4.1 and of AP in Figure 4.5, it is clear that the AP has a much higher burning rate at similar flame strain rates.

Chapter 5

Conclusions

The concept of a reverse hybrid rocket motor having a solid oxidizer and gaseous fuel was examined using pressurized counterflow, strand, and static-fired rocket motor experiments. A simple performance analysis comparing several HC/AP systems with a classical HTPB/LOX hybrid and HTPB/AP composite solid propellant systems suggest the HC/AP reverse hybrid should yield theoretical specific and density specific impulse values similar to a composite solid propellant, with density specific impulse values exceeding the classical hybrid system due to the high density of AP. High density benefits system performance as an increase in the propellant mass fraction may permit greater payload capacity.

For comparison and system validation purposes, regression rates of HTPB and GOX were determined at varied pressures using a counterflow burner contained within a windowed pressure vessel. The results agreed well with published literature at atmospheric pressure, showing regression rates from 0.08 to 0.28 mm/s for strain rates ranging from 350 to 1500 1/s. Further analysis for pressures up to 4.32 MPa showed that the regression rate was independent of pressure when examined as a function of momentum flow rate.

Burning rates of solid AP pellets with gaseous ethylene were determined as functions of pressure and strain rate using a counterflow burner contained within a windowed pressure vessel. Results show a weak dependence of the burning rate on flame strain rate at low pressures, with the burning rate increasing by 40% when the strain rate was increased by over 200%. This dependence was observed to decrease with increasing pressure, with burn rates at high pressures becoming nearly independent of the strain rate over the range of fuel flow rates considered. At these high pressures, the burning rates were in agreement with published data for pure AP.

Furthermore, for pressures ranging from 0.1 to 6.5 MPa, the burning rates exhibit several distinct burning regimes. Under low pressure conditions (below 1 MPa) the decomposition process is driven by heat transfer from the diffusion flame to the AP surface. With increasing pressure, the diffusion flame remains unaffected, while chemical reaction rates between AP decomposition product species increase, driving the monopropellant flame closer to the AP surface accelerating pellet decomposition. Under high pressure conditions (pressures above 3 MPa), the burning rates are controlled by the monopropellant flame and are nearly unaffected by the presence of the diffusion flame, explaining the minimal dependence on flame strain rate. Similar studies conducted in each of the three regimes using methane as the gaseous fuel suggest an independence of the AP burning rate on fuel type.

Static-fired motor experiments demonstrated that under low initial pressures (0.1 and 1.1 MPa), the reverse hybrid system does not reach the high burning rate regimes, resulting in a slow, low pressure burn. Increasing the initial pressure to 2.2 to 4.2 MPa resulted in a brief ignition delay followed by a progressive burn. The effect of fuel flow rate was also examined by varying the mass flow of fuel from 0.29 to 6.3 g/s. This showed that a lower limit to fuel flow exists, below which the motor will not operate in the high pressure, high burning rate regimes. The results suggest that such a reverse hybrid is feasible, though further work is necessary to fully understand the system and optimize motor operation and performance.

References

1.   Sutton, G.P. and Biblarz, O., (2010) *Rocket Propulsion Elements*, 8th ed., New York: John Wiley and Sons Inc.

2.   Marxman, G.A. and Gilbert, M., (1963) Turbulent Boundary Layer Combustion in the Hybrid Rocket, *Symposium (International) on Combustion*, 9(1), pp. 371-383.

3.   Sims, J.R. and Christensen, H.C., (1965) Investigation of Binderless Reverse Hybrid Propellant Systems, *Naval Ordinance Test Station, China Lake, CA*.

4.   Smooke, M.D., Yetter, R.A., Parr, T.P., Hanson-Parr, D.M., Tanoff, M.A., Colket, M.B., and Hall, R.J., (2000) Computational and Experimental Study of Ammonium Perchlorate/Ethylene Counterflow Diffusion Flames, *Proceedings of the Combustion Institute*, 28(2), pp. 2013-2020.

5.   (2001) ICT Database of Thermochemical Values.

6.   Lemmon, E.W., McLinden, M.O., and Friend, D.G., Thermophysical Properties of Fluid Systems, in P.J. Linstrom and W.G. Mallard, Eds., *NIST Chemistry WebBook, NIST Standard Reference Database Number 69*, Gaithersburg, MD: National Institute of Standards and Technology. Retrieved June 3, 2012 from http://webbook.nist.gov.

7.   Risha, G.A., (2003) *Enhancement of Hybrid Rocket Combustion Performance Using Nano-Sized Energetic Particles*, Ph.D. Dissertation, The Pennsylvania State University.

8.   Chiaverni, M.J., Serin, N., Johnson, D.K., Lu, Y.-C., Kuo, K.K., and Risha, G.A., (2000) Regression Rate Behavior of Hybrid Rocket Solid Fuels, *Journal of Propulsion and Power*, 16(1), pp. 125-132.

9.   Evans, B., Favorito, N.A., Boyer, E., Risha, G.A., Wehrman, R.B., and Kuo, K.K., (2004) Characterization of Nano-Sized Energetic Particle Enhancement of Solid-Fuel Burning Rates in an X-Ray Transparent Hybrid Rocket Engine, *40th AIAA/ASME/SAE/ASEE Joint Propulsion Conference and Exhibit*, AIAA Paper No. 2004-3821.

10.   Kuo, K.K., Risha, G.A., Evans, B.J., and Boyer, E., (2004) Potential Usage of Energetic Nano-sized Powders for Combustion and Rocket Propulsion, *Symposium on Synthesis, Characterization and Properties of Energetic/Reactive Nanomaterials held at the 2003 MRS Fall Meeting*.

11.   Young, G., Risha, G.A., Miller, A.G., Glass, R.A., Connell, T.L., and Yetter, R.A., (2010) Combustion of Alane-Based Solid Fuels, *International Journal of Energetic Materials and Chemical Propulsion*, 9(3), pp. 249-266.

12. Risha, G.A., Miller, A.G., Glass, R.A., Yeager, V.A., Chiaverni, M.J., and Tappan, B.C., (2011) Regression Rates of Solid Fuels Containing High Nitrogen (HiN) Materials, *47th AIAA/ASME/SAE/ASEE Joint Propulsion Conference and Exhibit*, AIAA Paper No. 2011-5912.

13. Karabeyoglu, M.A., Cantwell, B.J., and Altman, D., (2001) Development and Testing of Paraffin-based Hybrid Rocket Fuels, *37th AIAA/ASME/SAE/ASEE Joint Propulsion Conference and Exhibit*, AIAA Paper No. 2001-4503.

14. Karabeyoglu, M.A., Zilliac, G., Cantwell, B.J., DeZilwa, S., and Castellucci, P., (2004) Scale-Up Tests of High Regression Rate Paraffin-Based Hybrid Rocket Fuels, *Journal of Propulsion and Power*, 20(6), pp. 1037-1045.

15. Philmon, G., Krishnan, S., Varkey, P.M., Ravindran, M., and Ramachandran, L., (2001) Fuel Regression Rate in Hydroxyl-Terminated-Polybutadiene/Gaseous-Oxygen Hybrid Rocket Motors, *Journal of Propulsion and Power*, 17(1), pp. 35-42.

16. Frederick Jr., R.A., Moser, M.D., Whitehead, J., and Knox, L.R., (2005) Regression Rate Study of Mixed Hybrid Propellants, *41st AIAA/ASME/SAE/ASEE Joint Propulsion Conference & Exhibit*, AIAA Paper No. 2005-3545.

17. Young, G., Roberts, C., and Dunham, S., (2012) Combustion Behavior of Solid Oxidizer/Gaseous Fuel Diffusion Flames, *50th AIAA Aerospace Sciences Meeting including the New Horizons Forum and Aerospace Exposition*, AIAA Paper No. 2012-1127.

18. Bennet, D.P., Jr., *Inverse Hybrid Rocket*, United States Patent No. 3,555,826, Jan. 19, 1971.

19. Bennet, D.P., Jr., *Propulsion Method in an Inverse Hybrid Rocket Motor*, United States Patent No. 3,714,783, Feb. 6, 1973.

20. Kaufman, M.H., O'Drobinak, J.D., and Dake, J.O., Jr., *Hybrid Propellant System*, United States Patent No. 3,640,070, Feb. 8, 1972.

21. Chu, J.C., *Controllable Solid Propulsion System*, United States Patent No. 3,732,693, May 15, 1973.

22. Ortolani, C., Casci, C., and Chiesi, F., (1971) An Experimental Rocket Engine with Solid Oxidizer in Eutectic of Ammonium Nitrate-Ammonium Perchlorate, *Israel Journal of Technology*, 9(6), pp. 607-611.

23. Peretz, A., Miller, N., and Roni, Z., (1996) Hydrazine-based inverse hybrid engine for space applications, *32nd AIAA/ASME/SAE/ASEE Joint Propulsion Conference and Exhibit*, AIAA Paper No. 1996-2593.

24. St. Clair, C.P., Rice, E.E., Knuth, W.H., and Gramer, D.J., (1998) Advanced Cryogenic Solid Hybrid Rocket Engine Developments: Concept and Test Results, *34th AIAA/ASME/SAE/ASEE Joint Propulsion Conference and Exhibit*, AIAA Paper No. 1998-3508.

25. Gordon, S. and McBride, B.J., (1996) Computer Program for Calculation of Complex Chemical Equilibrium Compositions and Applications, *June 1996*.

26. Hill, P.G. and Peterson, C.R., (1992) *Mechanics and Thermodynamics of Propulsion*, 2nd ed., Reading: Addison-Wesley Publishing Company.

27. Jackson, V.E., Dixon, D.A., and Christe, K.O., (2012) Thermochemical Properties of Selenium Fluorides, Oxides, and Oxofluorides, *Inorganic Chemistry*, 51(4), pp. 2472-2485.

28. Oommen, C. and Jain, S.R., (1999) Ammonium Nitrate: A Promising Rocket Propellant Oxidizer, *Journal of Hazardous Materials*, 67(3), pp. 253-281.

29. Boggs, T.L., (1970) Deflagration Rate, Surface Structure, and Subsurface Profile of Self-Deflagrating Single Crystals of Ammonium Perchlorate, *AIAA Journal*, 8(5), pp. 867-873.

30. Atwood, A.I., Boggs, T.L., Curran, P.O., Parr, T.P., Hanson-Parr, D.M., Price, C.F., and Wiknich, J., (1999) Burning Rate of Solid Propellant Ingredients, Part 1: Pressure and Initial Temperature Effects, *Journal of Propulsion and Power*, 15(6), pp. 740-747.

31. Personal communication with Dr. Alice Atwood in July 2012.

32. Adams, G.K., Newman, B.H., and Robins, A.B., (1961) The Combustion of Propellants Based Upon Ammonium Perchlorate, *8th Symposium (International) on Combustion*, 8(1), pp. 693-705.

33. Friedman, R., Nugent, R.G., Rumbel, K.E., and Scurlock, A.C., (1957) Deflagration of Ammonium Perchlorate, *Symposium (International) on Combustion*, 6(1), pp. 612-618.

34. Hightower, J.D. and Price, E.W., (1967) Combustion of Ammonium Perchlorate, *Symposium (International) on Combustion*, 11(1), pp. 463-472.

35. Boggs, T.L., Zurn, D.E., and Netzer, D.W., (1973) Ammonium Perchlorate Combustion: Effects of Sample Preparation; Ingredient Type; and Pressure, Temperature and Acceleration Environments, *Combustion Science and Technology*, 7(4), pp. 177-183.

36. Puri, I.K. and Seshadri, K., (1986) Extinction of Diffusion Flames Burning Diluted Methane and Diluted Propane in Diluted Air, *Combustion and Flame*, 65(2), pp. 137-150.

37. Chelliah, H.K., Law, C.K., Ueda, T., Smooke, M.D., and Williams, F.A., (1990) An Experimental and Theoretical Investigation of the Dilution, Pressure, and Flow Field Effects on the Extinction Condition of Methane-Air-Nitrogen Diffusion Flames, *23rd Symposium (International) on Combustion*, 23(1), pp. 503-51145.

38. Parr, T.P., Hanson-Parr, D.M., Smooke, M.D., and Yetter, R.A., (2002) Ammonium Perchlorate/(H-2+CO) Gaseous Fuel Diffusion Flame Studies, *Proceedings Of The Combustion Institute*, 29(2), pp. 2881-2888.

39. Parr, T.P., Hanson-Parr, D.M., Smooke, M.D., and Yetter, R.A., (2005) AP/(N-2+C2H2+C2H4) Gaseous Fuel Diffusion Flame Studies, *Proceedings Of The Combustion Institute*, 30(2), pp. 2113-2121.

40. Tanoff, M.A., Ilincic, N., Smooke, M.D., Yetter, R.A., Parr, T.P., and Hanson-Parr, D.M., (1998) Computational and Experimental Study of Ammonium Perchlorate Combustion in a Counterflow Geometry, *27th International Symposium on Combustion*.

41. Seshadri, K. and Williams, F.A., (1978) Laminar Flow Between Parallel Plates With Injection of a Reactant at High Reynolds Number, *International Journal of Heat and Mass Transfer*, 21(2), pp. 251-253.

42. Chiaverni, M.J., Kuo, K.K., Peretz, A., and Harting, G.C., (2001) Regression-Rate and Heat-Transfer Correlations for Hybrid Rocket Combustion, *Journal of Propulsion and Power*, 17(1), pp. 99-110.

43. Cengel, Y.A. and Cimbala, J.M., (2010) *Fluid Mechanics: Fundamentals and Applications*, 2nd ed., New York: McGraw-Hill.

44. Risha, G.A., Son, S.F., Yetter, R.A., Yang, V., and Tappan, B.C., (2007) Combustion of Nano-Aluminum and Liquid Water, *Proceedings Of The Combustion Institute*, 31(2), pp. 2029-2036.

45. Connell, T.L., Santi, S.A., Risha, G.A., Muller, B.A., and Batzel, T.D., (2009) Experiment and Semi-Empirical Modeling of Lab-Scale Hybrid Rocket Performance, *45th AIAA/ASME/SAE/ASEE Joint Propulsion Conference and Exhibit*, AIAA Paper No. 2009-5086.

46. Risha, G.A., Yetter, R.A., Yang, V., Malchi, J.Y., and Sabourin, J.L., (2005) Assessment of Nano-Powder Rare Earth and Transitional Metal Oxides on Energetic Reactions, *Interim Report, October 25, 2005*.

47. Glassman, I. and Yetter, R.A., (2008) *Combustion*, 4th ed., New York: Elsevier Inc.

48. Arden, E.A., Powling, J., and Smith, W.A.W., (1962) Observations on the Burning of Ammonium Perchlorate, *Combustion and Flame*, 6(3), pp. 21-33.

49.   Beckstead, M.W., Derr, R.L., and Price, C.F., (1970) A Model of Composite Solid-Propellant Combustion Based on Multiple Flames, *AIAA Journal*, 8(12), pp. 2200-2207.

50.   Lengelle, G., Duterque, J.R., Godon, J.C., and Trubert, J.F., (1991) Solid Propellant Steady Combustion - Physical Aspects, *Combustion of Solid Propellants*: AGARD-LS-180, pp. 3-1 - 3-25.

Appendix A

Calibrations

Pressure Transducer

      The pressure transducers utilized in this work were Setra Model 206 differential pressure transducers with ranges of 0-1000 psig and 0-3000 psig. Each transducer was calibrated using a calibration apparatus that allowed simultaneous measurement of the transducer signal via a BNC output and the pressure via mechanical gauges with 0.25% uncertainties over the full pressure range. If necessary after allowing the transducer to warm up, the transducer was re-zeroed to bring the initial voltage to 0.1 VDC at 0 psig prior to calibration. Pressure was then supplied to the calibration apparatus in increments to provide at least ten points throughout the full range of the transducer. A linear fit was then applied to the points to determine the actual pressure as a function of output signal voltage for each transducer.

Orifice Discharge Coefficient

      The flow control orifices used for regulating gas flows into the pressurized counterflow burner and rocket motor were constructed of stainless steel tubing that had one end rounded and closed off. The orifice hole was laser-cut into this face by Lenox Laser, and then the orifice tube was inserted into a compression fitting to allow it to be connected to the experiment gas lines. Each orifice was calibrated (similar to the method used by Risha [7]) in order to determine its discharge coefficient (C_D). This was done so accurate calculations of gas flow could be made from Equation (3), where $\dot{m}_{actual}$ is mass flow, P is pressure upstream of the orifice, A_t is the orifice throat area, γ is the ratio of specific heats of the gas, R is the universal gas constant, MW is the gas molecular weight, and T is temperature.

$$\dot{m}_{actual} = C_D \frac{PA_t\gamma}{\sqrt{\gamma \frac{R}{MW}T}} \sqrt{\left(\frac{2}{\gamma+1}\right)^{\frac{\gamma+1}{\gamma-1}}} \tag{3}$$

In order to calibrate the orifices, two orifices were connected in series as shown in Figure A.1, with a calibrated pressure transducer reading the upstream pressure of each orifice. By locating the smaller of the two orifices upstream and supplying a sufficient upstream pressure, both orifices could achieve a choked flow condition. By assuming conservation of mass such that the mass flow through the smaller orifice is equal to the mass flow through the larger orifice, and knowing the discharge coefficient and dimension of one of the orifices, the discharge coefficient could be determined for the second orifice. The system was thoroughly checked for leaks that might affect the conservation of mass assumption prior to calibration.
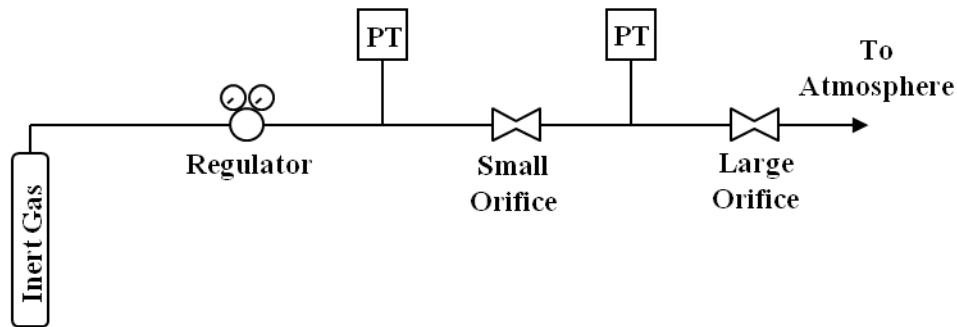

Figure A.1. Orifice discharge coefficient calibration schematic.

Mass Flow Meter

Electronic mass flow meters were utilized for generating mass flow correlations for ethylene and methane as functions of flow conditions and controlling orifice size. Calibrations for the flow meters were obtained by directly measuring the volume flow of a gas with a bubble meter and the correlating that to the 0 to 5 VDC output signal voltage. Gas correction factors provided by the manufacturers were utilized to convert from volume flow of the calibrated gas to other gases that the flow meter would be controlling. The validity of these correction factors

were checked by directly measuring both gases at certain flow rates and comparing to the correction factor predictions. Atmospheric conditions from the time of calibration and gas properties were then employed to obtain linear correlations of gas mass flow as a function of meter signal voltage. High flow meters were calibrated by overlapping their range with lower flow meters that had been calibrated directly.

Choked Flow of Fuel and Ideal Gases

The gaseous fuels selected for this study often enter their supercritical regimes at conditions found during counterflow tests and rocket motor firings. For ethylene, these conditions are often just above the critical temperature and/or pressure, where its properties begin to deviate significantly from the ideal gas model, resulting in a non-linear dependence of density on pressure. Due to this deviation, the ideal gas assumptions used in choked flow equations no longer permit accurate determination of mass flow rates, requiring an empirical fit to be generated as functions of orifice size and upstream pressure. This fit was produced by varying the upstream pressure, then recording pressure and using flow-calibrated mass flow meters to measure mass flow rates. Based on classical choked flow relations, the measured mass flow rate was then normalized by C_D and the orifice throat area, assuming a linear dependence on area. This assumption was verified by testing various orifices sizes and generating a polynomial fit to the normalized mass flow rate as a function of upstream pressure. The results are presented in Figure A.2 in addition to the ideal gas model, with the resulting choked flow relation for ethylene provided in Equation (4).

$$\dot{m} = C_D A_t [2.4346 P^4 - 22.948 P^3 + 86.365 P^2 + 137.40 P + 11.382] \tag{4}$$

Here $\dot{m}$ is the mass flow through the orifice in grams per second, A_t is in square centimeters, and P is in megapascals.
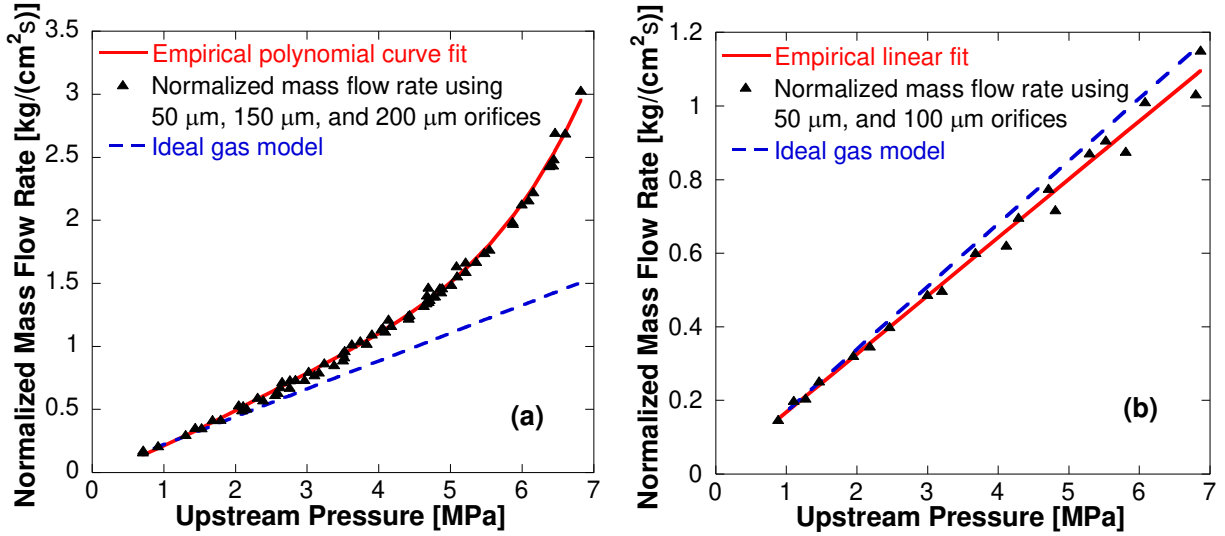

Figure A.2. Empirical fits for normalized ethylene (a) and methane (b) mass flow rates.

While methane also transitions to a supercritical fluid for conditions under which this study was performed, the critical temperature of methane is 190.564 K, which is well below the test conditions, resulting in a linear dependence of density that agreed well with the ideal gas model in Equation (3). A similar analysis was performed for methane to determine the choked mass flow rate at varying upstream pressures, and is plotted in Figure A.2, with the resulting

$$\dot{m} = C_D A_t [158.04 P + 10.342] \qquad (5)$$

choked flow equation for methane provided in Equation (5). As in the previous equation, $\dot{m}$ is in grams per second, A_t is in square centimeters, and P is in megapascals.

The mass flow rates of the ideal gases used in this study were determined through classical choked flow analysis using Equation (3) and the calibrated orifices described earlier.

Velocities at the exits of the flow tubes for all gases considered were then computed using $\dot{m}$ = ρuA, where u is the average flow velocity and A is the exit area of the tube.

Additionally, correlations were obtained for ethylene and methane to determine the mass flow through an orifice when the flow unchoked. The apparatus used for this correlation is shown in Figure A.3 and is similar in principle to the apparatus used for determining the orifice discharge coefficient. Adjusting the metering valve effectively varies the size of the downstream orifice, such that when the metering valve is smaller than the upstream orifice, the flow through the upstream orifice unchokes. The amount of normalized mass flow relative to choked flow was then plotted as a function of the ratio of the pressure downstream of the orifice to the pressure upstream of the orifice. A polynomial curve fit was then generated for both gases, as shown in Figure A.4.
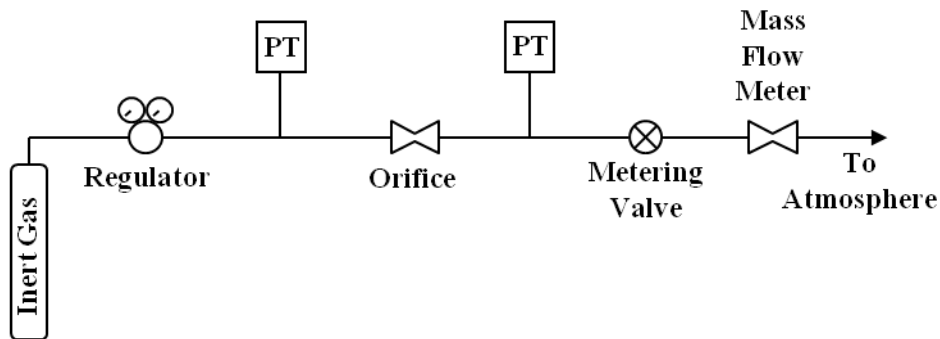
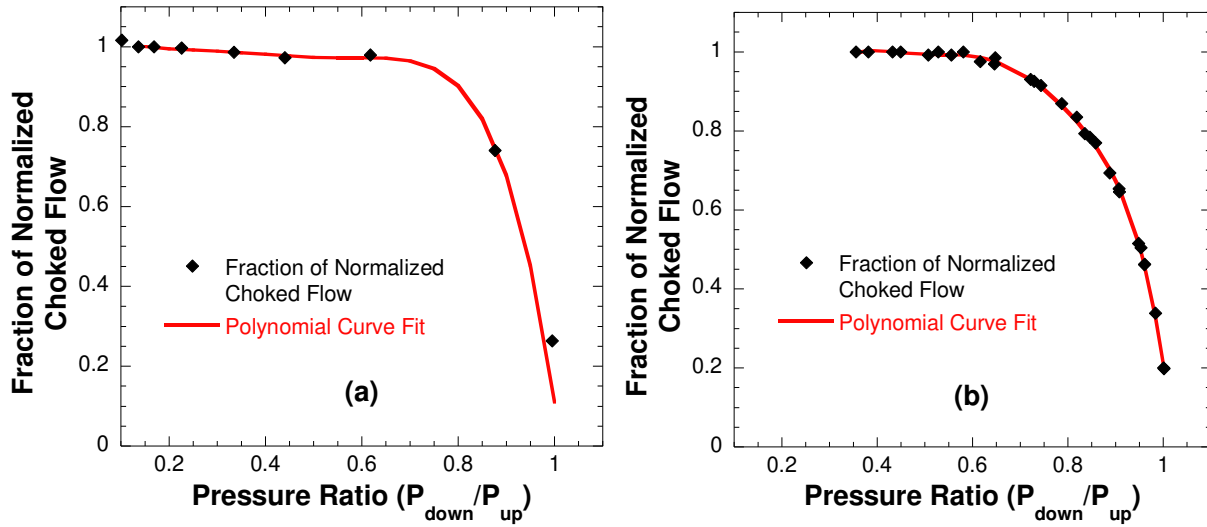Figure A.3. Schematic of unchoked flow correlation apparatus.

Figure A.4. Empirical mass flow correlations for unchoked flow through an orifice for (a) ethylene and (b) methane as a function of pressure ratio.

LVDT

The LVDT was calibrated by fixing it in place and then depressing the tip with a high precision linear measurement instrument. Initial calibrations were performed using a mill capable of resolving movement to 0.013 mm (0.0005 in.). After the pressurized counterflow system had been assembled, subsequent calibrations were performed using an optical translation stage fixed to the burner assembly that was capable of resolving 0.025 mm (0.001 in.). Careful attention was paid to the LVDT supply voltage as testing showed that there was a noticeable change in the signal output with supply voltages ranging from 11 VDC to 15 VDC. Ten points were taken across the range of the LVDT to generate a linear calibration curve for displacement as a function of output signal voltage.

Load Cell

The load cells for measuring thrust in the reverse hybrid rocket motor firings utilized a TMO-1 amplifier to condition the raw load cell signal for recording with the data acquisition system. The load cells and TMO-1 were zeroed and calibrated prior to testing and calibration checks were performed throughout the testing process. The cells were loaded with several different known weights in order to obtain a linear calibration for force as a function of output signal voltage. The output of the load cell was noted to drift over the course of a day, but calibration checks confirmed that the slope of the calibration curve remained essentially the same, allowing thrust measurements to be offset by the "zero" value at the beginning of a test.

Appendix B

SolidWorks Drawings

Pellet Holder
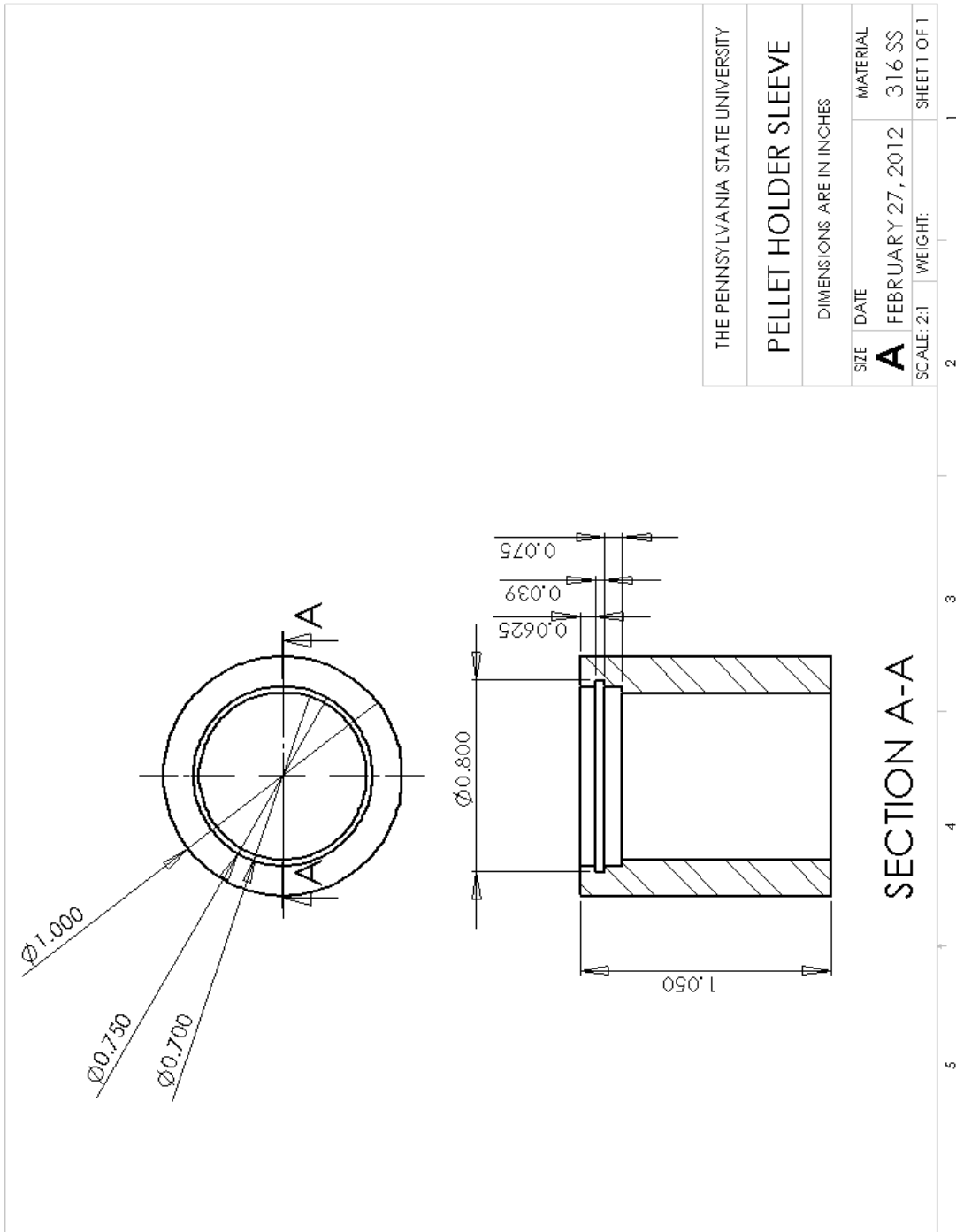
Figure B.1. Drawing of sleeve component of pellet holder base for the pressurized counterflow burner

0.750

0.375

0.750

0.375

∅0.315

4 × ∅ 0.201 ▽ 0.650
1/4-20 UNC ▽ 0.500

∅0.404
∅0.474
∅0.700
∅0.500
∅0.700
∅0.315

∅1.500
∅0.700
∅0.616

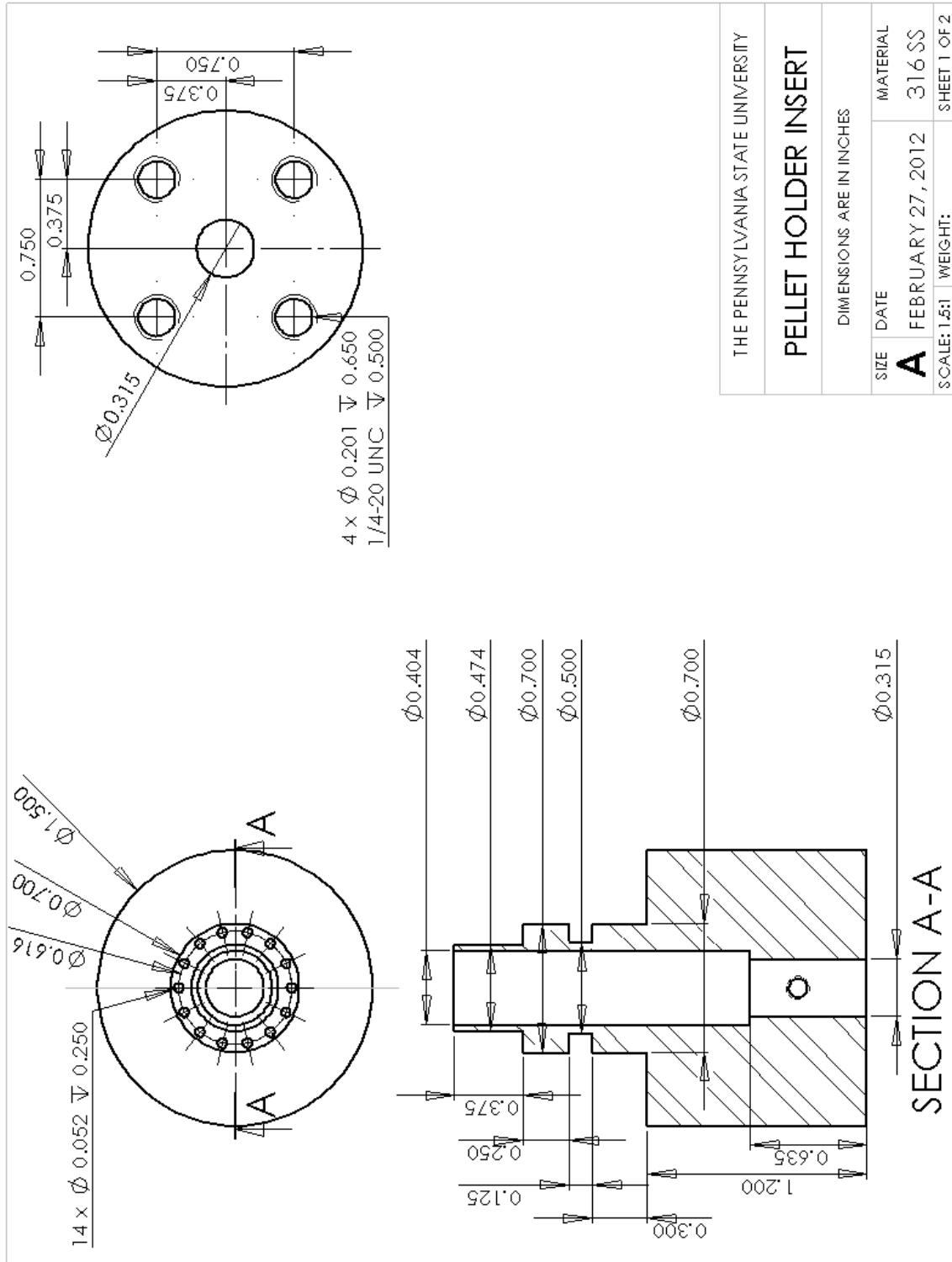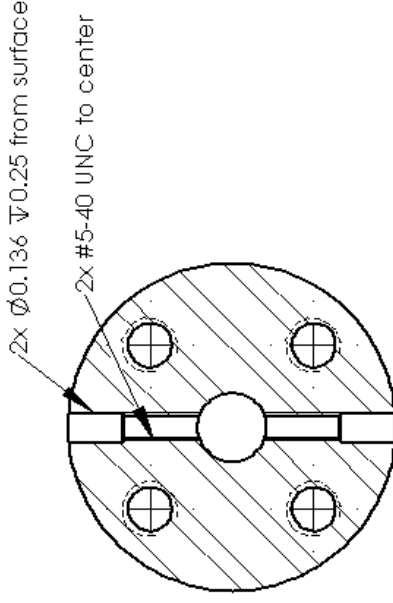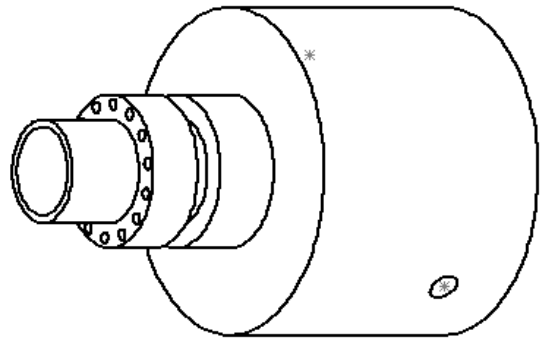14 × ∅ 0.052 ▽ 0.250

A
A

0.375
0.250
0.125
0.300
1.200
0.635

SECTION A-A

Figure B.2. Drawing of the insert component of pellet holder for the pressurized counterflow burner.

52
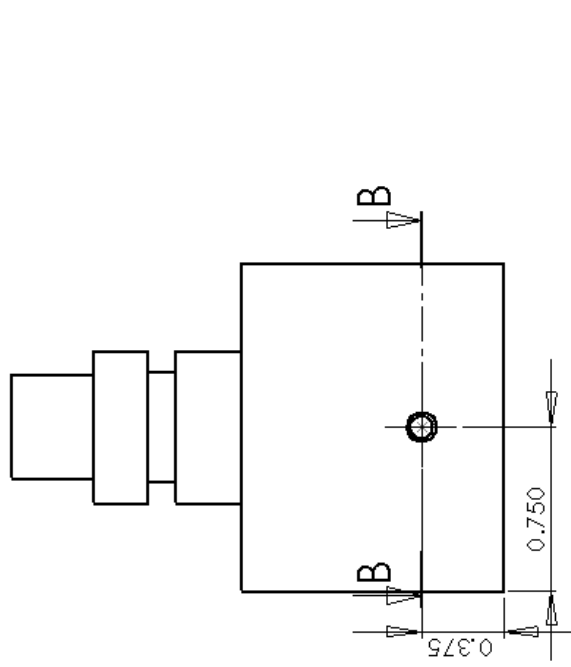
THE PENNSYLVANIA STATE UNIVERSITY

PELLET HOLDER INSERT

DIMENSIONS ARE IN INCHES

SIZE	DATE	MATERIAL
A	FEBRUARY 27, 2012	316 SS
	SCALE: 1.5:1 WEIGHT:	SHEET 2 OF 2

2x Ø0.136 ▽0.25 from surface

2x #5-40 UNC to center

0.750

0.375

SECTION B-B

Figure B.3. Drawing of set screw holes in insert piece of pellet holder for the pressurized counterflow burner.

Weld sleeve to insert

2x Ø 0.3125 counterbore
to 0.55 from center plane

Drill 2x Ø0.144 ▽1.0 from counterbore surface
Removeable smaller part will have #8 close clearance
Larger part will have #8 tapped threads
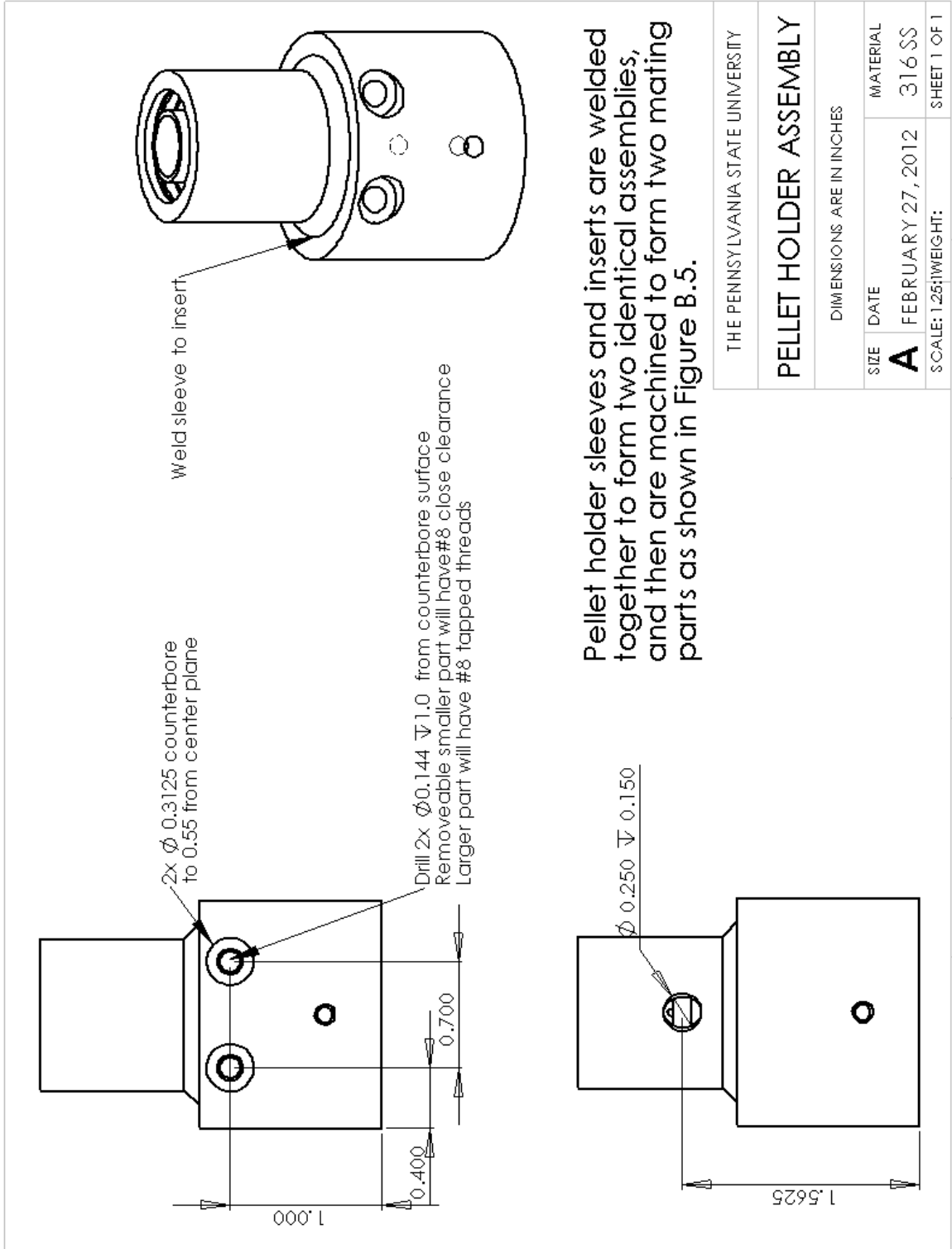
Pellet holder sleeves and inserts are welded
together to form two identical assemblies,
and then are machined to form two mating
parts as shown in Figure B.5.

0.700

0.400

1.000

Ø 0.250 ▽ 0.150

1.5625

Figure B.4. Drawing of assembly of pellet holder components for the pressurized counterflow burner.
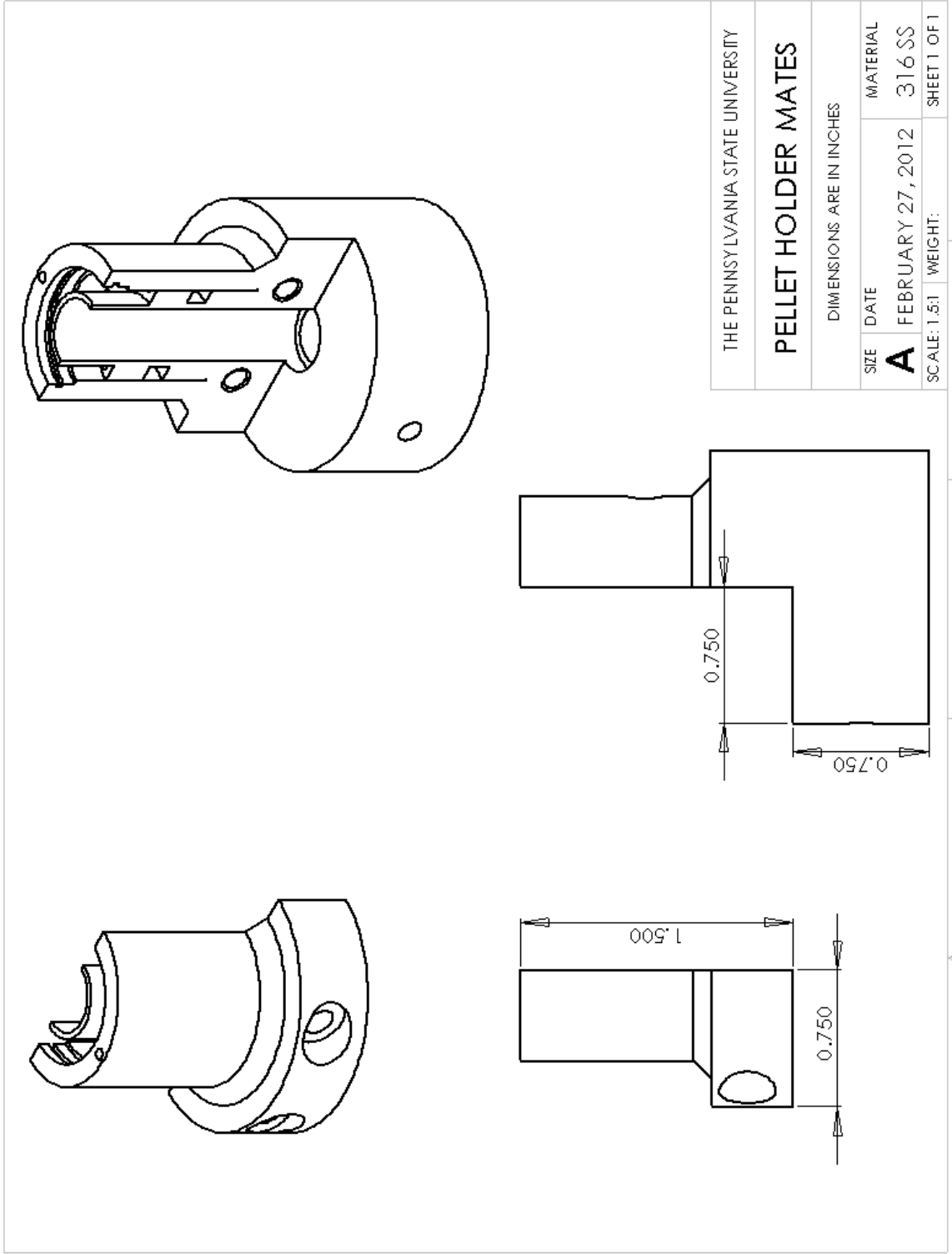
Figure B.5. Drawing of machined mating components of pellet holder assembly for pressurized counterflow burner.
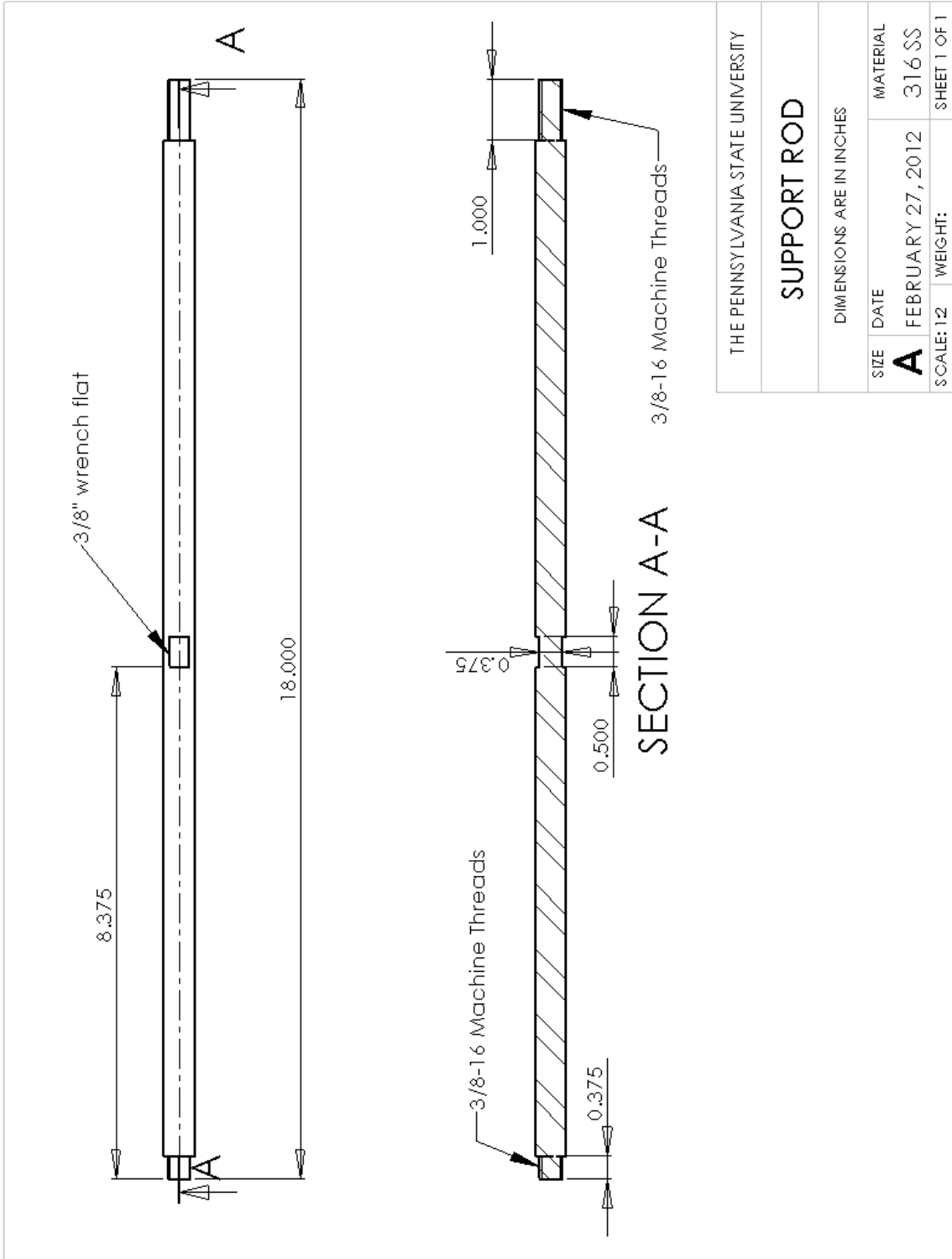
Standoff Rods

Figure B.6. Drawing of one of four support rods that hold counterflow pellet holder inside pressure vessel.

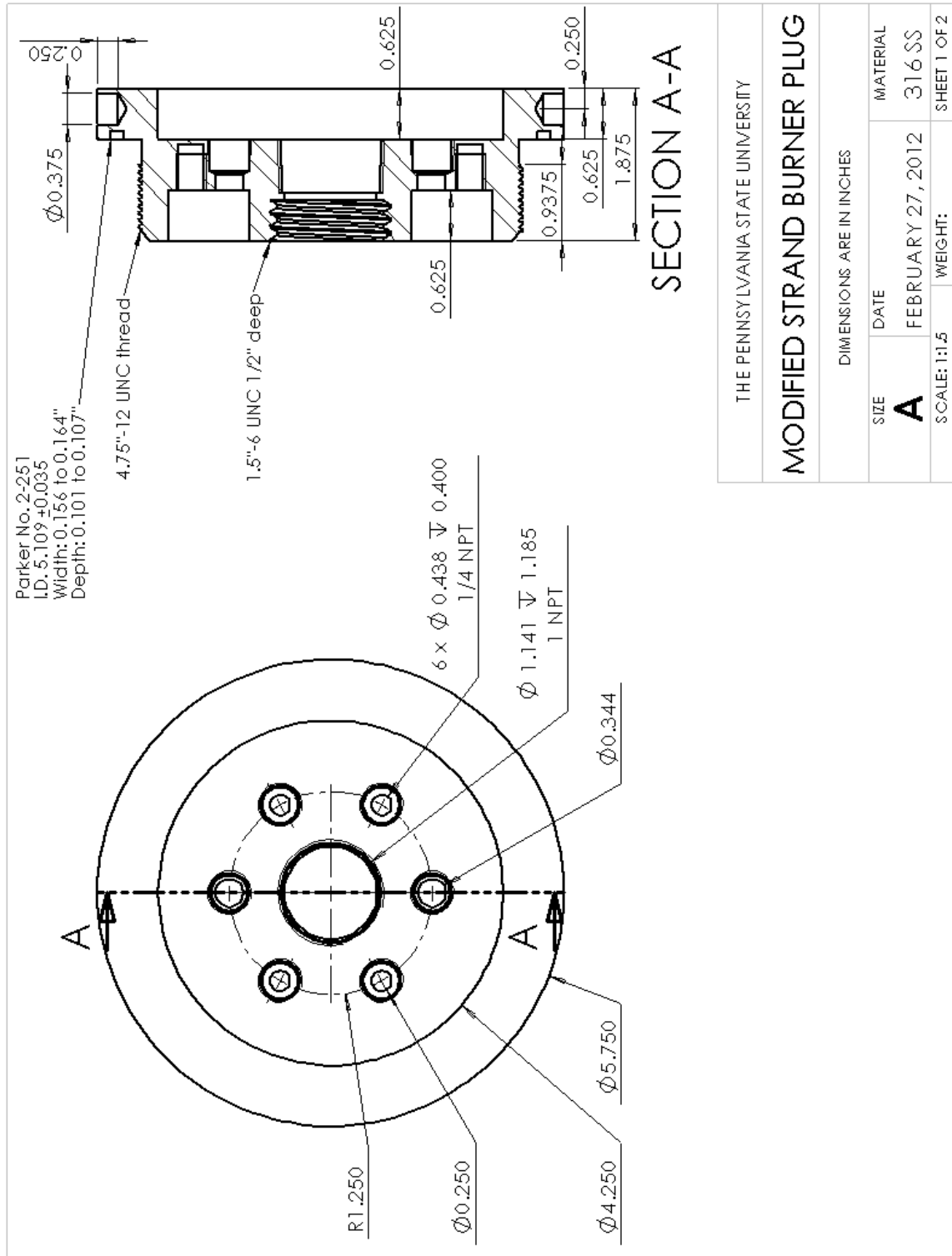**Modified Strand Burner Plug**

Figure B.7. Drawing of modifications to top of strand burner plug to accommodate counterflow burner system.
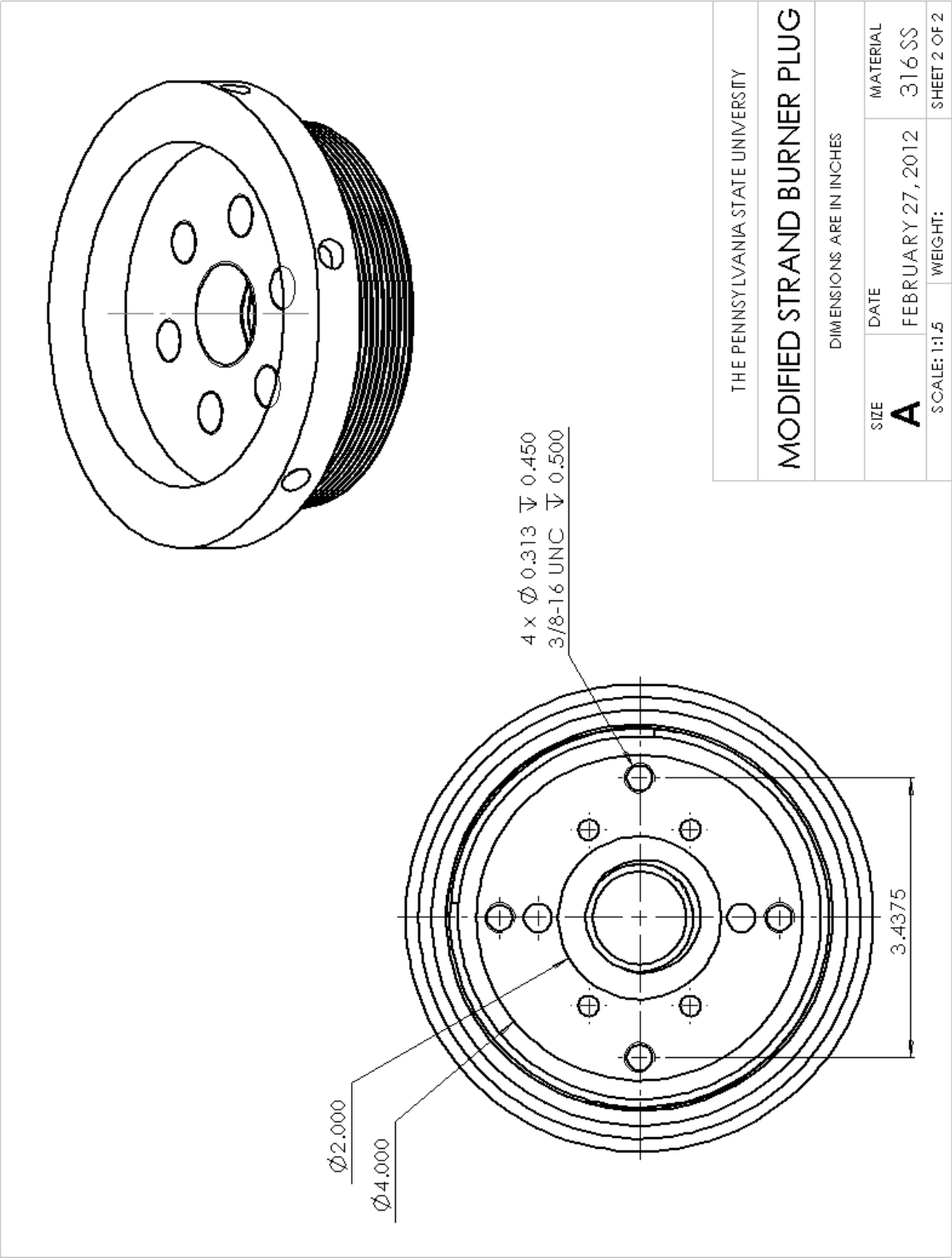
57

Figure B.8. Drawing of modifications to bottom of strand burner plug to accommodate counterflow burner.
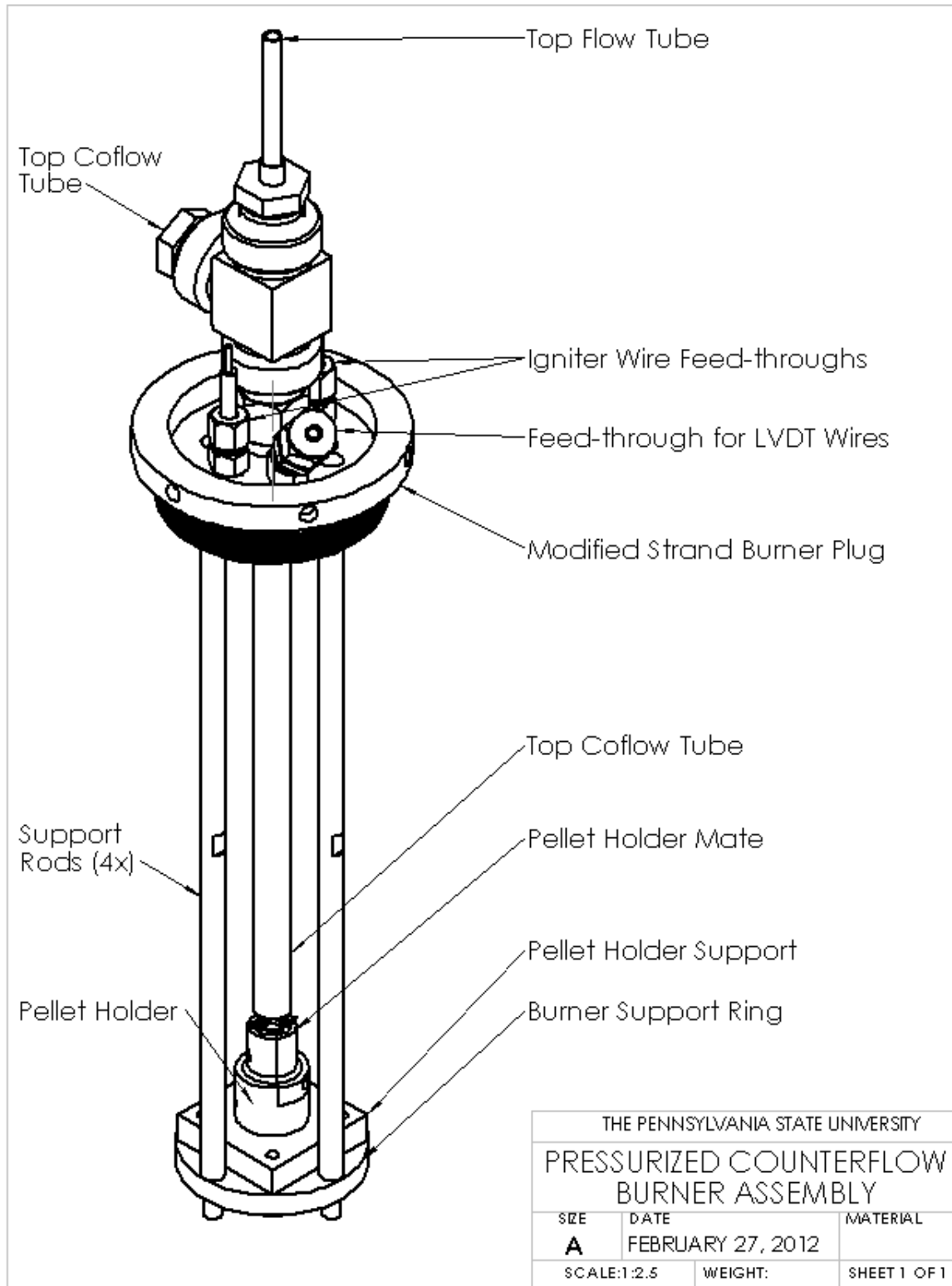
Pressurized Counterflow Assembly

Figure B.9. Drawing of pressurized counterflow burner assembly.